UNIVERSIDAD DE CONCEPCIÓN
FACULTAD DE CIENCIAS FÍSICAS Y MATEMÁTICAS

Chemistry in the Cradle: A Microphysical Study of Star-Forming Regions

Química en la cuna: un estudio microfísico de las regiones de formación estelar

Por: Gonzalo Ignacio Latrille Jaque

Tesis presentada a la Facultad de Ciencias Físicas y Matemáticas de la Universidad de Concepción para optar al grado académico de Magíster en Astronomía

Diciembre 2025
Concepción, Chile

Profesor Guía: Dr. Stefano Bovino

A Fundación 42

AGRADECIMIENTOS

Firstly, I would like to thank my supervisor and guide, Professor Dr. Stefano Bovino, and my co-supervisor, Dr. Alessandro Lupi, for their patience, continuous support despite the distance, their teaching, valuable feedback, and for always being kind to me throughout this long journey.

Quisiera agradecer a mi madre, Lenka, quien ha sido hasta el día de hoy el mayor apoyo emocional en mi vida y sin quien no estaría hoy en este segmento final. Muchas gracias por tu amor y cariño incondicionales, por estar siempre para mí, aconsejarme, confiar en mis capacidades, apoyarme y cuidarme, recordándome siempre por qué elegí este camino; así como también a mis hermanos, Vinko y Miguel, por apoyarme en toda esta etapa a pesar de la distancia que nos separa.

Por otro lado, no puedo sino agradecer a varias personas que han sido parte de este camino, comenzando con Scarllet, quien ha estado para mí en momentos difíciles y siempre recordándome que las cosas no son en blanco y negro, brindando calma con su serenidad; y también a mis amigos Andrés, Estefanía y Sergio, con quienes siempre puedo contar y en quienes siempre pienso cuando se trata de conversar y compartir.

Finalmente, y no menos importante, a mis perritas, Lulú y Piccolina, siempre brindando dosis grandes de serotonina al llegar a casa y que espero que nos sigan cuidando, incluso después de su partida.

Agradezco el financiamiento recibido por la Beca Magíster Nacional 2024 (código 2024-22241873) brindado por la Agencia Nacional de Investigación y Desarrollo (ANID).

Resumen

El estudio de la formación estelar comúnmente implica comprender la macrofísica, es decir, la evolución de la dinámica del gas a través de la contracción gravitacional, la difusión magnética y la hidrodinámica. Por otro lado, la microfísica, que aborda los aspectos de la composición intrínseca del gas, el polvo y la resolución, representa una herramienta fundamental para revelar la complejidad de las nubes moleculares, es decir, la cuna de las estrellas. Diversos estudios investigan componentes específicos de la formación estelar mediante un enfoque fragmentado, en el cual solo se incluyen los procesos importantes para los objetivos científicos, mientras que aquellos considerados menos relevantes se excluyen, principalmente porque añadirlos incrementaría de manera significativa el costo computacional.

Por lo tanto, la motivación de este proyecto es estudiar los efectos que surgen cuando se incluyen todos los procesos de la teoría de la formación estelar, tanto macrofísicos como microfísicos, con el fin de simular el entorno más completo posible. Entre los procesos que afectan la microfísica, el feedback estelar se vuelve relevante, como las supernovas, los outflows, la modulación estelar, la radiación desde el ultravioleta hasta el infrarrojo y los rayos cósmicos. Por un lado, se examinaron los efectos en la química de una nube molecular cuando se emplea un marco adecuado de propagación de rayos cósmicos, lo que conduce a diferencias significativas en trazadores moleculares clave sensibles a variaciones en la tasa de ionización por rayos cósmicos. Por otro lado, se desarrolló una nueva red química que incluye la química en las fases gaseosa y sólida, así como procesos inducidos por rayos cósmicos y radiación, con el objetivo de caracterizar químicamente una nube molecular gigante para futuras simulaciones numéricas que incorporarán todos los feedbacks estelares. Esta red muestra perfiles de abundancia prometedores para especies clave cuando se consideran procesos de radiación, mecanismos de enfriamiento y calentamiento.

Finalmente, se presentan los primeros resultados de la simulación inicial de una nube molecular gigante que incluye esta nueva red química.

Keywords – star formation, molecular clouds, molecular species, microphysics, methods: numerical

Abstract

The study of star formation commonly implies understanding macrophysics, that is, the evolution of gas dynamics through gravitational contraction, diffusion magnetism and hydrodynamics. On the other side, microphysics, which deals with the aspects of the intrinsic composition of the gas, dust, and resolution, represents a fundamental tool to unveil the complexity of molecular clouds, that is, the nursery of stars. Several studies investigate specific components of star formation in a fragmented approach, where only the processes important to the scientific goals are included, while those considered less relevant are excluded, mainly because adding them would significantly increase the computational cost.

Therefore, the motivation of this project is to study the effects that arise when all processes in star formation theory, both macrophysical and microphysical, are included in order to simulate the most complete environment possible. Among the processes that affect the microphysics, stellar feedback such as supernovas, outflows, stellar modulation, ultraviolet to infrared radiation, and cosmic rays becomes relevant. At one hand, the effects on the chemistry of a molecular cloud when a proper CR propagator scheme is employed were examined, leading to significant differences for key molecular tracers sensitive to variations in the cosmic-ray ionisation rate. On the other hand, a new chemical network that includes gas- and solid-phase chemistry, cosmic-ray and radiation chemistry was developed, aimed to chemically characterise a giant molecular cloud for further numerical simulations that will include all stellar feedbacks. This network shows promising abundance profile from key species when photo-processes, cooling and heating mechanisms are considered.

Finally, the first results of the initial simulation of a giant molecular cloud that includes this new chemical network are presented.

Keywords – interestellar medium, molecular clouds, cosmic rays, astrochemistry, molecules, star formation

Contents

List of Tables

List of Figures

Chapter 1

Introduction

1.1 Molecular clouds

The interstellar medium (ISM) primarily consists of several gas structures, such as diffuse clouds, dense clouds, reflection nebulae, gas bubbles, jet remnants. Among these, dense clouds, also known as molecular clouds (MCs) or dark clouds, serve as the birthplaces of stars. MCs exhibit several observable properties and cover a wide range of physical characteristics, with their irregular shape being the only consistent feature. Observations have identified MCs with sizes ranging from a few dozen to up to a hundred parsecs. When a MC reaches such a large size, it is classified as a giant molecular cloud (GMC), which is found almost exclusively in spiral arms (Ballesteros-Paredes et al., 2007) and is capable of hosting stellar clusters. The identified physical properties of these structures are as follows: gas temperatures of approximately $\sim$ 20 K at the edges and $\sim$ 8–10 K in the deepest and densest regions (Ballesteros-Paredes et al., 2007; Bergin and Tafalla, 2007); masses ranging from 10^3 to 10^6 $M_\odot$ (Ballesteros-Paredes et al., 2007; Bergin and Tafalla, 2007); high column densities of 10^{23}–10^{25} cm^{-2} (Bergin and Tafalla, 2007); and lifetimes of about $\sim 10^7$ yr (Larson, 1981; Schinnerer and Leroy, 2024).

The formation of molecular clouds is thought to occur through gas-phase transitions. It begins with the HI medium undergoing shock compression within the warm neutral medium (WNM), which subsequently leads to the formation of the cold neutral medium (CNM). For this process to be successful, the compression must occur at an angle below a critical threshold relative to the magnetic field

(MF) lines, allowing the density to increase sufficiently for molecular gas to form (Hennebelle and Inutsuka, 2019). As a result, molecular gas is expected to form within CNM structures, which are themselves embedded in the WNM, also referred to as the interclump medium.

The internal structure is hierarchical (Hennebelle and Inutsuka, 2019). Initially, clumps form, followed by the development of filamentary structures within them. Subsequently, dense cores arise inside these filaments, with up to 70-80% forming there (Hennebelle and Inutsuka, 2019). Once the cores accrete enough material to ignite protostars, envelopes appear around them. Throughout most of their structure, and as revealed by molecular line observations, MCs exhibit motions dominated by supersonic turbulence ($\mathcal{M} > 1$), particularly within filaments, while on subparsec scales, dense cores show subsonic turbulent motions ($\mathcal{M} < 1$) (Larson, 1981; Bergin and Tafalla, 2007; Hennebelle and Inutsuka, 2019). Most of the mass resides in low-extinction regions, indicating that it lies in low-density gas. In contrast, dense cores are compact regions, up to approximately 30.000 au in size, always located in high-extinction regions, indicative of high-density gas (Bergin and Tafalla, 2007). Although MCs can form many stars, only about 30% of their total mass reservoir is used in this process, and this fraction decreases as their size increases, reaching values as low as 1%. This trend can be explained by the fact that, when MCs are small, the available gas is confined within a limited volume, which facilitates the inward flow of material into the filaments that feed dense cores, thereby consuming more gas. In larger clouds, however, much of the gas does not flow inward toward the filaments; star formation is indeed a very inefficient process.

Turbulence is ubiquitous throughout the ISM, yet its complete understanding remains an open problem in star formation theory. It is inferred that its existence is due to the lack of systematic patterns, such as expansion, infall, or rotation, exhibiting a power-law relation between its velocity dispersion, σ, and its size L (Bergin and Tafalla, 2007). Different phases of the ISM exhibit distinct turbulence velocities (Larson, 1981; Bergin and Tafalla, 2007; Hennebelle and Inutsuka, 2019). For instance, dense cores are subsonic ($\mathcal{M} \lesssim 1$), clumps are supersonic ($\mathcal{M} \sim 5.3$), and the inter clump gas is highly supersonic ($\mathcal{M} \sim 53$). These turbulent motions are generally supersonic and compressible, and are believed to be of magnetohydrodynamic (MHD) nature (Hennebelle and Inutsuka,

2019). Turbulence can promote star formation by channeling infalling gas along magnetic field lines into regions with subsonic motions, acting as mass reservoirs for upcoming stars. Conversely, turbulence can inhibit star formation by exerting flow pressure that counteracts gravitational collapse (Hennebelle and Inutsuka, 2019).

Magnetic fields and gravity are other agents involved in the theory of star formation. The former is studied as a fluid behaving hydrodynamically. It is described as being 'frozen' into the non-magnetised fluid (neutral gas) of the ISM, moving together with the gas. Although this applies in the ideal case, corresponding to regions with both low density and extinction. Because of this, these regions can posses a high level of ionisation, allowing them to be approximately treated as ideal MHD. On the other hand, when regions have high extinctions, the degree of ionisation can drop to $\sim 10^{-7}$ due to gas shielding against radiation. Unlike the ideal case, the two fluids, magnetised and non-magnetised, composed of ionised and neutral species respectively, collide less frequently. These collisions lead to a gradual drag of the MF lines and a subsequent drift relative to the neutrals. The continuous drift of the field lines implies that the decoupling between the two fluids is high enough for neutrals to cross them perpendicularly. Therefore the field is no longer frozen into the gas. This phenomenon and correction of the ideal MHD is known as ambipolar diffusion (Hennebelle and Inutsuka, 2019).

The presence of MHD effects in filamentary structures acts as a mechanism that contributes to the preservation of the parent cloud. When gravity triggers contraction in high-density regions, MF can halt this contraction if it occurs perpendicular to the field lines, as the resulting increase in magnetic pressure counteracts gravity. Conversely, MHD effects and gravity can also complement each other, amplifying anisotropies in both the gas distribution and MHD turbulence, and even promoting the formation of filaments that can be sustained purely without self-gravitation. Through these MHD effects, MCs can extend their lifetime by increasing the free-fall time ($t_{\rm ff}$). If gravity were the only agent during the contraction, with pure thermal pressure opposing it, collapse within dense cores would proceed on the timescale set by $t_{\rm ff}$. However, its presence in the gas allows the cloud's lifetime to be extended by a factor of a few, for instance, 1.6 times (Hennebelle and Inutsuka, 2019).

The dispersal of MCs is still not fully understood, although it is thought to be closely related to their sizes. In smaller MCs, some studies suggest that stellar outflows (jets) can halt star formation by disrupting dense cores or even by completely dispersing the parent cloud. Another scenario involves the formation of open clusters, which can entirely disperse the parent cloud through stellar feedback and radiation. Similarly, globular clusters can destroy GMCs through mechanisms such as modulation and photo-heating, effectively dispersing them. These examples briefly illustrate that stellar feedback mechanisms play a central role in the destruction of the parent cloud.

1.2 Stellar feedback

Before the first generation of stars forms within MCs, the only processes acting in the cloud are turbulence, magnetic fields, and gravity. Once stars form, several additional processes arise in the ISM that influence star formation; these processes are collectively referred to as stellar feedback. Most of these feedback mechanisms can be classified as pre-supernova (pre-SN) feedback. After ignition, stars exert pre-SN feedback on the surrounding ISM, shaping its structure.

The entire physical process can be summarised as follows: protostars of all spectral types except O and B emit radiation pressure, non-ionising radiation, and stellar winds that can affect the parent cloud to a mild degree. Since these types of protostars lack ionising radiation, their light cannot penetrate far, heating only the immediate surrounding gas and dust (their envelopes) to several hundred kelvins. When outflow events occur, their impact depends on both the number of simultaneous events and the size of the cloud. The outcome can vary, ranging from the disruption of the entire cloud, to the perturbation by halting gas accretion or destruction of dense core sites, or the injection of turbulence into low-density gas. At ~ 4 Myr, when the first supernovae (SNe) explode, they can generate shock fronts due to the collision of ejected material with the surrounding gas, while also enriching the medium (Schinnerer and Leroy, 2024).

In the case of high-mass protostars, specifically types O and B, the consequences of their feedback are dramatically enhanced. In addition to radiation pressure and stellar winds, these stars emit ionising radiation (extreme UV), which strongly impacts and shapes the multi-phase ISM. During early stages and the first $\sim$

8 Myr (before SNe), massive protostars gradually form the Strömgren sphere. Initially, before the Strömgren sphere becomes noticeable, the surrounding gas is immediately heated to temperatures of $T \sim 10^6 - 10^8$ K by wind-driven shocks, producing X-ray emission. Then, almost simultaneously, the photoionised gas is strongly compressed by momentum injected from stellar winds and radiation pressure. As long as the dust shell of the birth site remains optically thick to UV photons, the extreme UV radiation cannot escape the sphere. In this phase, radiation transfers momentum to the gas, driving it outward and causing the Strömgren sphere to expand gradually. At some point, after the dust shell has dissipated, ionising radiation reaches equilibrium with the environment, halting the Strömgren sphere expansion while it is now referred as HII region. Then, the over-pressured ionised gas leaks through into the inhomogeneities of the ISM, particularly low-density regions, ultimately breaking out of the cloud. The ionising radiation follows the path traced by the leaked ionised gas, encountering little absorption or weakening by the already ionized material. As time passes, multiple "patches" form within the parental cloud due to the expansion of the over-pressured ionized gas into low-density regions. Finally, after ~ 8 Myr have passed, massive O- and B-type stars go SNe, ultimately dispersing the entire gas cloud (Schinnerer and Leroy, 2024).

1.3 Molecular physics

Molecular physics encompasses the chemistry and microphysics of the ISM. All gas structures, from large to small scales, are chemically characterised by atomic, molecular, and ionised species, which can serve as observational tools to infer and interpret the current state of a gas region. Chemical and numerical models are extensively used to reconstruct the history of MCs based on their present state. In addition, chemistry is important because it regulates gas cooling, thereby influencing star formation.

Since the ISM is multi-phase, each phase is characterised by its own chemical composition. Low-density regions are dominated primarily by atomic species, along with a comparable fraction of ionised atoms, due to their susceptibility to FUV radiation emitted by nearby stars. In contrast and unlike low-density regions, MCs can host molecules alongside atomic species. This is largely due

to the high concentration of CO near their envelopes, which absorbs incoming radiation and effectively shields these regions long enough to allow the formation of molecular species.

The chemical study of the ISM is highly complex and, above all, computationally expensive due to the large number of species involved. All chemical species within an environment interact with one another and therefore evolve together. The variation in the number density of a single species can be described using a system of ordinary differential equations (ODEs), constructed from all the chemical reactions in which it participates, whether contributing to its formation or to its destruction to form other species. Mathematically, this is represented as a Cauchy problem. These ODEs are referred as rate equations and are written as follows:

$$\frac{dn_i}{dt} = \sum_{j \in F_i} \left(k_j \prod_{r \in R_j} n_{r(j)} \right) - \sum_{j \in D_i} \left(k_j \prod_{r \in R_j} n_{r(j)} \right). \tag{1.3.1}$$

From Eq.(1.3.1), k_j is the rate coefficient, the first sum corresponds to all reactions forming n_i, while the second sum includes all reactions destroying n_i. The sets F_i, D_i, and R_j, encompass the complete collection of reactions in which n_i is involved, split into *formation* and *destruction*, and *reactants* of each corresponding reaction involved in F_i and D_i, respectively.

Within a chemical network, there are different types of reactions:
Formation of bonds

- Radiative association: $\mathrm{X} + \mathrm{Y} \longrightarrow \mathrm{XY} + h\nu$
- Associative detachment: $\mathrm{X}^- + \mathrm{Y} \longrightarrow \mathrm{XY} + \mathrm{e}^-$
- Grain surface: $\mathrm{X} + \mathrm{Y{:}g} \longrightarrow \mathrm{XY} + \mathrm{g}$

Destruction of bonds

- Photo-dissociation: $\mathrm{XY} + h\nu \longrightarrow \mathrm{X} + \mathrm{Y}$
- Dissociative recombination: $\mathrm{XY}^+ + \mathrm{e}^- \longrightarrow \mathrm{X} + \mathrm{Y}$
- Collisional dissociation: $\mathrm{XY} + \mathrm{M} \longrightarrow \mathrm{X} + \mathrm{Y} + \mathrm{M}$

Rearrangement of bonds

- Ion-molecule reactions: $\mathrm{X}^+ + \mathrm{YZ} \longrightarrow \mathrm{XY}^+ + \mathrm{Z}$

- Charge-transfer reactions: $X^+ + YZ \longrightarrow X + YZ^+$
- Neutral-neutral reactions: $X + YZ \longrightarrow XY + Z$

Unlike low-density regions, which consist almost entirely of gas-phase and are strongly affected by photo-processes with high collisional rates, high-density regions contain both gas-phase and a much more active solid-phase component. The solid-phase is named after the presence of dust grains, which provide an additional pathway for molecule formation, something that would be difficult to achieve through gas-phase reactions alone. The cores of dust grains are composed primarily of silicates or carbon, often with elongated morphologies and believed to contain cavities, with their size distribution following the expression $\frac{dn}{da} \propto a^{-3.5}$, which indicates that small dust grains are far more abundant than larger ones. Dust enables species to adsorb onto its surface and form more complex molecules. In this process, the dust absorbs the excess of energy released during reactions when species are in the transient complex state, examples include the formation of H_2 in both low- and high-density regions, and CH_3OH (methanol). It is believed that new molecules can form directly when a second reactant adsorbs onto the dust grain. Alternatively, it is also proposed that reactants may migrate across the dust surface through hopping or quantum tunnelling using their excess energy, eventually reacting and desorbing.

In high-density regions, where UV radiation is shielded and temperatures are extremely low, icy mantles can form on the surfaces of dust grains. Mantles are primarily composed of oxygen and oxygen-bearing species, such as H_2O. Carbon atoms also adhere to dust grains, reducing their abundance in the gas phase. As both carbon and oxygen are now part of the solid phase, sensitive species such as deuterium (D) and its derivatives can proliferate due to the reduced destruction channels normally related with C and O. Small grains are the main contributors to the additional solid-phase pathway, as they absorb the excess energy released during chemical reactions. They also contribute to cooling the environment by absorbing FUV photons produced by radiative association of certain species and re-emitting them as far-infrared (FIR) radiation.

1.3.1 Cosmic-ray ionisation rate

Cosmic rays (CRs) are charged, highly energetic particles that are ubiquitous in the ISM, composed mainly of protons, helium nuclei and heavier nuclei (such as carbon), which account for approximately 98%, with positrons (e^+) and electrons (e^-) accounting for the remainder. There is no strict upper limit in how energetic they can be, although it is typically described to range from 100 to 10^{25} eV, with their energies reflecting their likely origin: (i) local sources (10^9 - 10^{10} eV) such as stars; (ii) galactic sources (10^{10} - 10^{15} eV) such as SN remnants; (iii) extra-galactic sources (E>10^{15} eV) such as active galaxy nuclei. They propagate across the ISM following the MF lines, which makes it impossible to trace them back to their source of origin due to the diffusion transport along these lines. They can eventually be guided into high-density regions where, unlike in low-density environments, they transfer a substantial fraction (or even all) of their energy to the medium through collisions with gas. Microscopically, when they collide with gas, they interact with atomic and molecular species, playing a crucial role in environments strongly shielded from radiation (e.g., molecular clouds and prestellar cores). The energy deposited into gas particles is referred to as the cosmic-ray ionisation rate, which acts as a source of ionisation for all species, since none are immune to ionisation by cosmic rays. For this role, low-energy CRs are particularly important (E < 10^{12} eV), as high-energy CRs tend to traverse entire gas structures without interacting significantly with the gas (Padovani et al., 2018).

The degree of CR ionisation rate in these environments has been the subject of intense study in recent years, so much that it led to the launch of the Voyager 1 and 2 spacecraft since the solar modulation made such observations impossible from Earth. The study and modelling (slow-down continuum approximation) initiated in Padovani et al. (2009) and further refined in Padovani et al. (2018) and Padovani et al. (2022), which considered observations conducted from the spacecraft, ultimately led to the theoretical models $\mathscr{H}$ (the average CR ionisation rate on diffuse media), $\mathscr{L}$ (from the data of the two Voyager spacecraft), and $\alpha = -1.2$ (representing an upper limit to the CR ionisation rate estimates in diffuse region), as shown in Fig. (1.3.1), with the majority of observational estimates from various environments lying between these models. Furthermore, the CR ionisation rate is inversely proportional to column density, indicating that CRs

undergo attenuation when they traverse increasingly column densities. This leads to the introduction of the effective column density, $N_{\rm eff}$, which accounts for the accumulated column density that has been traversed by CRs.

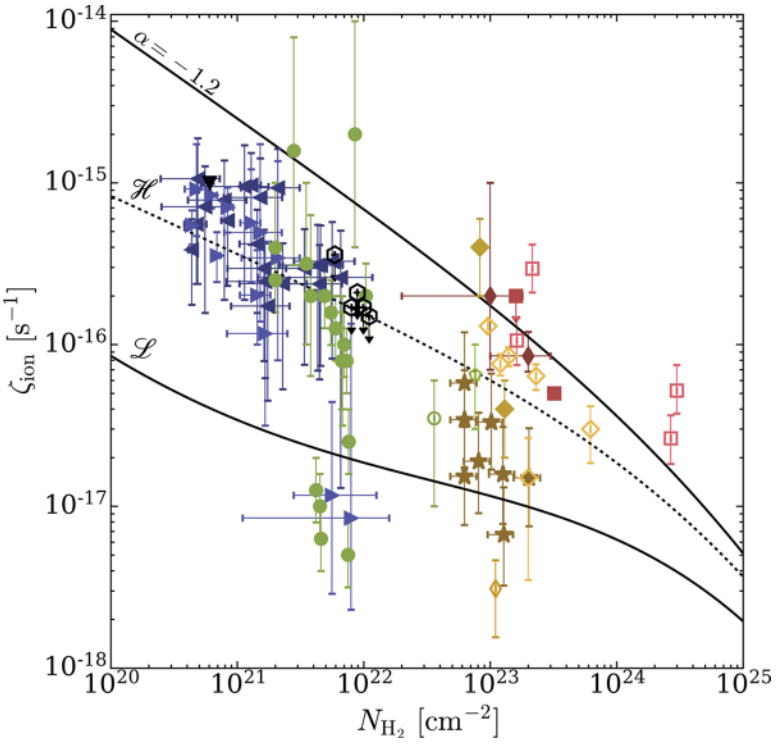

Figure 1.3.1: Figure from Padovani et al. (2022), which shows the the total cosmic-ray ionisation rate as a function of H_2 column density, with the theoretical models $\mathscr{H}$, $\mathscr{L}$ and $\alpha = -1.2$. It also shows observational estimates in diffuse clouds shown as downward-pointing triangle (Shaw et al., 2008), left-pointing triangle (Indriolo and McCall, 2012), and right-pointing triangle (Neufeld and Wolfire, 2017). Observational estimates in low-mass dense cores are shown as solid circles (Caselli et al., 1998), empty hexagons (Bialy, Shmuel et al., 2022), an empty circle (Maret and Bergin, 2007), and an empty pentagon (Fuente et al., 2016). Observational estimates in high-mass star-forming regions are shown as stars (Sabatini et al., 2020), solid diamonds (de Boisanger et al., 1996), empty diamonds (van der Tak et al., 2000), empty thin diamonds (Hezareh et al., 2008), and solid thin diamonds (Morales Ortiz et al., 2014). Observational estimates in circumstellar discs are shown as solid squares (Ceccarelli et al., 2004), and in massive hot cores as empty squares (Barger and Garrod, 2020).

Cosmic rays propagate in a spiral around the paths defined by the MF lines. Consequently, the pitch angle, defined as the angle between the velocity vector and the line (ω), becomes particularly relevant when CRs encounter the edges of a high-density region. Since the shape and configuration of the line field can be complex and its strength may exceed the typical interstellar value by orders

of magnitude (Crutcher, 2012), it converge toward denser central regions. As a result, the line density increases and the pitch angle grows in response. On the one hand, if ω exceeds a critical value, $\omega_{\rm crit}$, incoming CRs are reflected back in a process known as the magnetic mirroring effect. In such cases, the ionisation rate produced by the mirrored CRs is expected to be low (Padovani et al., 2013). On the contrary, when CRs satisfy $\omega < \omega_{\rm crit}$, the convergence of the field lines generates a magnetic focusing effect, enhancing the concentration of CRs in that region.

In environments such as MCs, low-energy CRs play a key role by driving ion–neutral reactions and ionising neutral species such as H_2, N_2, and CO. Since molecular hydrogen is the most abundant species, most of the cosmic-ray ionisation rate is directed towards it, producing H_2^+. This ion subsequently reacts with another H_2 molecule to form H_3^+, which is regarded as a cornerstone of ion–molecule chemistry. It initiates the formation of other molecules, including HCO^+, OH^+ ions, the molecular form of atomic species such as O_2 and N_2, complex neutrals such as H_2O and NH_3, and deuterated species such as H_2D^+. Similarly, its isotopologue H_2D^+ triggers the deuteration pathway, leading to the formation of species such as DCO^+ and N_2D^+ in the medium. For this reason, it has been proposed that the imprint of the CR ionisation rate is linked to specific cations in the environment (HCO^+, DCO^+) that are highly sensitive to variations in the ionisation rate.

1.3.2 Physical description

In general, many of the chemical reactions occurring in the ISM proceed via collisions and their rate coefficient, k, can be described by the Modified Arrhenius formula:

$$k(T) = A(T/300)^B e^{-C/T}, \tag{1.3.2}$$

where T is temperature and A, B, C are coefficients. There is a particular type of collisional reaction that cannot be described by 1.3.2, due to its independence from the environment and the high kinetic energy of one of the reactants, CRs.

In this case, the rate coefficient expressed as

$$k = a_0 \zeta, \tag{1.3.3}$$

here ζ is the cosmic-ray ionisation rate of either H or H_2 (common in dense regions and referred to as ζ_2) and a_0 is a dimensionless scale factor different for each species. Similarly, photoreactions are treated as uni-molecular reactions (analogous to CR reactions) and are typically described using the Draine equation,which is given as

$$k = k_0 e^{-\gamma A_v}, \tag{1.3.4}$$

with k_0 as the unaffected radiation field, and A_v as the visual extinction, and the exponential term accounts for the continuum attenuation by the dust.

Additionally, the *Kinetic Database for Astrochemistry* (KIDA; Wakelam et al., 2012) recommends two rate coefficients based on the capture approach proposed by Su and Chesnavich (1982) for ion-neutral reactions with dipole moment that have no measured coefficients. These rate coefficients are intended to cover the full range of temperatures at which a reaction can occur, from low to high, respectively:

$$k(T) = \alpha\beta(0.62 + 0.4767\gamma(300/T)^{0.5}), \tag{1.3.5}$$

$$k(T) = \alpha\beta\left(1 + 0.0967\gamma(300/T)^{0.5} + \frac{\gamma^2}{10.526}\frac{300}{T}\right), \tag{1.3.6}$$

with a, b, c being the branching ratio of the reaction, the Langevin rate, and an auxiliary parameter that takes into account the temperature at 300 K, respectively.

1.3.2.1 Ortho-para relevance

Molecular hydrogen can have two different spin states, ortho and para, which depend on the alignment of the nuclear spins of the protons: parallel in the ortho state and antiparallel in the para state. The ortho state is more abundant at high temperatures, whereas the para state dominates at low temperatures. Due to this, the ortho–para state of the molecule can be used to infer the thermal state of a gas cloud (Gavilan et al., 2012), with the ortho–para ratio (OPR) quantifying the relative populations of the two states. At high temperatures, the OPR converge to the statistical ratio 3, while for low temperatures it decreases to

as low values as 10^{-4} (Lupi et al., 2021). The initial value of the OPR is crucial for understanding the chemical composition of collapsing gas, particularly for its level of deuteration (Flower et al., 2004). Furthermore, the initial OPR strongly influences the abundance of species in low temperature regions such as molecular clouds (Flower et al., 2006), such as H_3^+.

1.3.3 Thermodynamics

In the ISM, the thermodynamics is governed by cooling and heating mechanisms that determine the energy balance.

Microscopically, cooling occurs when species absorb energy from the gas and subsequently emit it as photons through spontaneous emission, a process driven by collisional excitation between species. Similarly, collisional ionisation constitutes another cooling mechanism: an electron is ejected as a result of collisions between species, followed by electronic recombination between such free electron and ionised species (H^+, H_3^+), which ultimately removes the excess kinetic energy via spontaneous emission. Conversely, heating occurs when species transfer energy to the gas. This can happen either through collisions or photoionisation, where an electron released from an atom or molecule and subsequently heats the gas through a process known as thermalisation, produced by elastic collisions between the electron and other species. For both heating and cooling, the total abundance (or density) of the species involved in these processes is crucial. Macroscopically, since heating involves species embedded in the gas, witch the gas coupled to the fluid motion, while cooling occurs primarily through radiation, the combined effect of both processes can be viewed as a moving, illuminated fluid.

The total cooling in MCs arises from mechanisms involving both atomic and molecular species. In particular, given that MCs are environments with low kinetic energy, gas cooling occurs through the rotational transitions of molecules, which provide a more efficient cooling mechanism than atomic transitions. At the edges of MCs, where CO is present, the isotopologues ^{12}CO and ^{13}CO dominate the cooling because of the high CO abundance (second most abundant after H_2; Tielens, 2005). Inside MCs, dust contributes to gas cooling by absorbing UV radiation generated by ion-neutral reactions (or by FUV in photo-dominated region) and re-emitting it as IR radiation.

Within MCs, the total heating is mostly dominated by CR heating. Furthermore, due to the lack of external radiation, CRs become the only external source of heating. The second major contribution to the total heating arises from the formation of H_2 on dust grains, which transfers part of the remaining excess of energy after desorption into the gas via collisions, thereby raising the gas temperature.

There are additional processes contributing to the total energy balance outside MCs, which are strongly determined by the current state of ISM. On the cooling side, CII and OI are responsible in radiatively cooling the gas in the neutral medium, while CI, SI, SiII, FeI, FeII also contribute to a mild degree. In ionised regions, radiative cooling is mainly driven by species such as OII, OIII, NII, SI, and SII, mainly through collisions with electrons. On the heating side, the photoelectric effect is the dominant heating mechanism in the neutral medium. This process involves the ejection of an e^- with a high excess of energy from the surface of dust grains after the absorption of energetic photons. Gas-dust collisions can also heat the gas as long as the dust is warmer than the gas. In HII regions, photoheating becomes a significant source of heating. Additionally, X-ray heating caused by hot gas and SNe also contribute to gas heating. CRs owing to their ubiquitous presence in the ISM, contribute to the total heating of all phases, but are dominant only within MCs (Tielens, 2005; Krumholz, 2015).

Chapter 2

Computational methods

2.1 Gas cloud simulations

To simulate gas cloud structures, such as GMCs, the module STARFORGE (STAR FORmation in Gaseous Environments, Grudić et al., 2021) will be employed. Its physical framework is implemented in GIZMO (Hopkins, 2015), specifically in the multi-method, multiphysics N-body and magnetohydrodynamic simulation suite. GIZMO was selected since it offers several and useful advantages for star formation problems. Among its features, its second-order, Galilean-invariant, Lagrangian meshless finite-volume magnetohydrodynamic methods; a spatially adaptive gravity solver, which works consistently with magnetohydrodynamics; and its own meshless discretisation and reconstruction schemes, which provide a flexible framework for incorporating additional physics not integrated in the core algorithms, such as diffusion, conduction, radiative transfer, stellar feedback, and non-ideal magnetohydrodynamic terms. Furthermore, GIZMO employs a powers-of-two time-stepping scheme integrated in all equations to follow processes in a wide range of timescales from ~ 1 yr to ~ 10 Myr.

The STAFORGE framework follows the approach of previous Lagrangian 3D star formation simulations (Klessen and Burkert, 2000; Bate et al., 2003). it discretises the mass gas structure and the surrounding medium into discrete elements of mass (Δm) and integrates their evolution in time according to the MHD equations. At certain stage, the MHD equations can no longer be accurately followed at the centres of runaway core collapse, these centres are therefore replaced with sink

particles (Bate et al., 1995), which represent protostars and can interact with the gas via gravity, accretion, and, if necessary, feedback. The core algorithms for star formation include solvers for magnetohydrodynamics, gravity, sinks-growth criteria, stellar feedback for jets, stellar winds, supernovae, and radiation, among others.

Magnetohydrodynamics

The main magnetohydrodynamic algorithm employed is the Meshless Finite Mass (MFM) method from Hopkins and Raives (2016). It discretises the fluid into several number of gas cells, each with mass ΔM_i, where each cell actually represents a certain volume $V_i = \Delta M_i/\rho_i$ determined via the M4 cubic spline kernel volume partition (Hopkins, 2015). The partition defines the effective face areas $A_{gg'}$ between each interacting pair of gas cells g and g', where the MHD equations evolve according to the following expression:

$$\frac{\mathrm{d}}{\mathrm{d}t}(VU)_{\mathrm{g}} = \sum_{rmg'} A_{\mathrm{gg'}} \cdot F_{\mathrm{gg'}}, \tag{2.1.1}$$

where $(VU)_{\mathrm{g}}$ represents conserved quantities such as mass, momentum, energy, among others, integrated over the volumetric domain defined by $A_{\mathrm{gg'}}$ of the cell, with $F_{\mathrm{gg'}}$ being the tensor of their fluxes. The fluxes are obtained by solving the Riemann problem using the reconstructed fluid states at the interface, according to the gradient estimator of the algorithm. These interfaces vanish naturally due to the MFM method, which follows the motion of the fluid elements. To avoid complex volume partitions arising from complicated shapes formed by the cells, the algorithm defines two useful effective cell sizes: the equivalent cell side length for a cubic cell of the same volume and mass:

$$\Delta x_{\mathrm{g}} = V_{\mathrm{g}}^{1/3} = \left(\frac{\Delta m_{\mathrm{g}}}{\rho_{\mathrm{g}}}\right)^{1/3} \approx 0.03 \text{ pc} \left(\frac{\Delta m}{10^{-3}\mathrm{M}_\odot}\right)^{1/3} \left(\frac{n_{\mathrm{H,g}}}{10^3 \text{ cm}^{-3}}\right), \tag{2.1.2}$$

and the volume-equivalent spherical radius:

$$h_{\mathrm{g}} = \left(\frac{3\Delta m_{\mathrm{g}}}{4\pi\rho_{\mathrm{g}}}\right)^{1/3} \approx 0.02 \text{ pc} \left(\frac{\Delta m}{10^{-3} \text{ M}_\odot}\right) \left(\frac{n_{\mathrm{H,g}}}{10^3 \text{ cm}^{-3}}\right), \tag{2.1.3}$$

with $n_{\mathrm{H,g}}$ being the number density of H set to $0.7\rho_{\mathrm{g}}/m_{\mathrm{p}}$, and 10^{-3} $\mathrm{M}_{\odot}$ being the mass resolution of STARFORGE.

Gravitation

The gravity solver in STARFORGE considers two cases: one for gas cells and another for small structures such as stars. On one side, the solver determines the gravitational field $g = -\nabla$, tidal tensor $T = -\nabla\nabla$ with $= \nabla^{-2}4\pi G\rho$ being the gravitational potential, and the gravitational jerk j, at the position of every gas cell and sink particle. To solve each formula, the algorithm first subdivides the entire domain of the simulation into an oct-tree structure, which then uses the monopole approximation to obtain the field contribution from each tree node. On the other side, when sink particles appear in the simulation, or when gas cells approach each other within their radii, a softened form of the gravitational force is employed to conserve the total linear and angular momentum. The softening for interactions between gas cell is fully adaptive, with the softening radius $S_i = H_i$, where H_i as the kernel radius. This ensures consistency between the gravitational force resolution and the cell volume partition used in the MHD equations, thereby preventing unphysical effects caused by mismatched hydrodynamical and gravitational resolutions. In the case of sink particles, softening addresses issues arising from close binary stars. Such binaries can impose a computational bottleneck due to very short orbital periods. Therefore, the softened radius for sink particles is simply set to a fixed radius S_{sink}, which is large enough to accurately follow collisional dynamics on spatial scales $\gtrsim S_{\mathrm{sink}}$, while limiting the close separation of binaries.

Sink particles

The formation of sink particles represents a star or protostar, used to model accretion, dynamics, and feedback. Each sink particle is located in a region of the simulation where the physical processes are unresolved and are therefore treated using sub-grid prescriptions. STAFORGE particularly implements sink particles alongside with physically motivated rules governing their for actions such as forming, accreting, merging with other sinks, and feedback. Sink formation effectively occurs when all of the following criteria are satisfied:

(i) The gas cell is denser than the density threshold, ρ_{th}, defined as the maximum

density of marginal Jeans resolution given as:

$$\rho_{\rm j} = 3 \times 10^{-14}\ {\rm g\ cm^{-3}} \left(\frac{\Delta m}{10^{-3} {\rm M}_\odot} \right)^{-2} \left(\frac{c_{\rm s}}{0.2\ {\rm km\ s^{-1}}} \right)^{6}, \tag{2.1.4}$$

with the local gas sound speed c_s.

(ii) Overlap with pre-existing sink is forbidden. A certain gas cell must be the densest among all neighbouring gas cells or sink particles with kernel radii overlapping.

(iii) The density of the gas cell is increasing as $\Delta \cdot v < 0$, according to the same gradient estimator of the algorithm used to reconstruct fluid quantities.

(iv) The gas cell is gravitationally unstable at the resolution scale (Federrath et al., 2010; Hopkins et al., 2013). To assess this, the algorithm evaluates the local virial parameter of the gas cell:

$$\alpha_{\rm g} = \frac{\frac{2\pi^2}{\Delta x^2}(c_{\rm s}^2 + v_{\rm A}^2) + \|\Delta v\|^2}{4\pi G \rho}, \tag{2.1.5}$$

with $\Delta x = (\Delta m/\rho)^{1/3}$ is the local cell length, and $\|\cdot\|$ denotes the Frobenius norm. This conditions is satisfied only if a gas cell is $\alpha_{\rm g} > 2$.

(v) The tidal tensor T is fully compressive at the location of the gas cell.

(vi) The gas cell can indeed collapse before being accreted, determined when the local gas free-fall time $t_{\rm ff} = \sqrt{\frac{3\pi}{32 G \rho_{\rm g}}}$ is shorter than both the time-scale for approaching a sink particle and the orbital time-scale around that sink particle, given respectively by the following expressions:

$$t_{\rm c,min} = \min_{s' \neq s} \frac{\sqrt{r_{ss'}^2 + \epsilon_{\rm star}^2}}{v_{ss'}}, \tag{2.1.6}$$

$$t_{\rm dyn,min} = \min_{s' \neq s} \sqrt{\frac{(r_{ss'}^2 + \epsilon_{\rm star}^2)^{3/2}}{G(m_s + m_s')}}, \tag{2.1.7}$$

with $\epsilon_{\rm star} = h_{\rm star}/2.8$ is the Plummer-equivalent sink softening radius, and $r_{ss'}$, $v_{ss'}$, M_s, $m_{ss'}$ are the separation, relative velocity, and respective masses of the sink particles s and s'.

Once a gas cell satisfies all conditions, it becomes a sink particle.

Gas accretion onto sink particles occurs through the accretion of gas cells. As with sink formation, accretion proceeds only if the gas cells satisfy the following criteria:

(i) The centre of gas cells approaches within the sink radius $R_{\rm sink}$, where $R_{\rm sink}$ is defined as the greater of the sink particle softening ,radius $S_{\rm star}$, or the volume-equivalent radius of a gas cell at the density corresponding to marginal Jeans resolution, given by:

$$R_{\rm sink} = \max\left(S_{\rm star}, 0.79\frac{G\Delta m}{c_{\rm s}^2}\right) \tag{2.1.8}$$

$$= \max\left(S_{\rm star}, 18\ {\rm au}\left(\frac{\Delta {\rm m}}{10^{-3}\ {\rm M}_\odot}\right)\left(\frac{{\rm c_s}}{0.2\ {\rm km\ s^{-1}}}\right)\right) \tag{2.1.9}$$

where $c_{\rm s}$ denotes the isothermal sound speed at the sink formation.

(ii) The sink and gas cell are gravitationally bound, which is evaluated using the following expression:

$$2u_{\rm g} + v_{\rm A,g}^2 + |v_{\rm g} - v_{\rm s}| < v_{\rm esc}^2 = -2(r_{\rm gs}), \tag{2.1.10}$$

where u_g is the specific internal energy of the gas, $v_{\rm A,g}$ is its Alfvén speed, and (r_{gs}) is the softened gravitational potential of the sink evaluated at the separation between the gas and sing r_{gs}.

(iii) The orbit of a gas cell lies within $R_{\rm sink}$, which occurs when the gas cell possesses less angular momentum than that of a circular Keplerian orbit around the sink at r_{gs}

$$|(x_g - x_s) \times (v_g - v_s)|^2 < G m_s r_{gs}. \tag{2.1.11}$$

(iv) Only gas cells with spatial resolution on the scale of $R_{\rm sink}$ can be accreted, given by the evaluation of their volumes:

$$V_g = \frac{m_g}{\rho_g} < \frac{4\pi}{3} R_{\rm sink}^3. \tag{2.1.12}$$

Merging between sink particles is possible, although it occurs only a few times out of $\gtrsim 1000$ stars. Sink particles can merge if the binary semimajor axis is less than $R_{\rm sink}$ and the secondary has a mass less than $10\Delta m$.

2.1.0.1 Stellar feedback

STARFORGE has been implemented with the stellar feedback from jets, stellar winds, supernovae, and radiation. Each feedback mechanism is incorporated into the algorithm either through local injection or cell spawning, as explained below.

On the one hand, the local injection approach (Hopkins et al., 2018) consists of constructing a new effective face, $A_{\rm b}$, which is formed from those gas cells in which their kernel radius, $H_{\rm b}$, contains the sink particle, and for which the kernel radius of the sink particle, $H_{\rm a}$, contains the centre of gas cells, expressed as $|x_a - x_b| < \max(H_{\rm a}, H_{\rm b})$. The local injection then proceeds by calculating the flux of quantities into the effective area, $A_{\rm b}$, towards the respective neighbouring gas cell, determined by the subtended angle to that side. On the other hand, the cell spawning procedure (Torrey et al., 2020) is introduced when the local injection faces challenges in its determination or represents a limitation. The first case occurs when the constructed effective face is large, so that it no longer serves as a good approximation; the second case arises when jets have larger subtended angles than those delimited by the effective face $A_{\rm b}$, which is common. New cells are always spawned in multiples of two, following the criteria set by each feedback when appropriate, with the distance between the centre of the spawned cell and sink particle given by:

$$R_{\rm spawn} = \min(R_{\rm sink}, \Delta x_s/2), \tag{2.1.13}$$

where Δx_s is the average inter-cell spacing in the vicinity of the sink. Spawned cells are assigned an initial temperature of 10^4 K, with their initial radial direction and velocity set according to the specifications of each feedback mechanism.

The physical description and numerical implementation of each stellar feedback mechanism are as follows:

(i) Jets remain an active area of research, and their physics and accurate models are still under study. Consequently, the modelling is based on a

simple phenomenological prescription from Cunningham et al. (2011), who parametrises the properties of jets using three parameters: the fraction of mass accreted by the envelope-disc-star system that is deflected into the jet, $f_{\rm w}$; the fraction, $f_{\rm K}$, of the Keplerian velocity at the protostellar radius, $R_{\rm star}$, at which jets are launched, such that

$$v_{\rm jet} = f_{\rm K}\sqrt{\frac{GM_{\rm star}}{R_{\rm star}}}, \tag{2.1.14}$$

and the collimation angle, θ_0, such that the angular distribution of injected wind momentum is given by the expression

$$\xi(\theta, \theta_0) = \left(\ln\left(\frac{2}{\theta_0}\right) \sin^2\theta + \theta_0^2 \right)^{-1}, \tag{2.1.15}$$

where θ is the angle with respect to the angular momentum axis of the sink $J_{\rm s}$. The defaults choices in the algorithm follow those suggested by Cunningham et al. (2011), with $f_{\rm w} = f_{\rm K} = 0.3$ and $\theta_0 = 0.01$. The numerical implementation of this feedback is carried out by the cell spawning procedure. It is activated once the mass in the jet reservoir is sufficient in order to spawn two cells of mass $\Delta M_{\rm W}$, with the angular direction relative to the sink angular momentum, $J_{\rm s}$, sampled randomly for the first cell according to Eq. (2.1.15), while the second cell points in the opposite direction to conserve both momentum and centre of mass.

(ii) Stellar winds, like jets, are the subject of intensive research, and accurate models for their treatment are still lacking, thereby their implementation follows a phenomenological description. Firstly, only stars with masses above 2 $\rm M_\odot$ are able to inject stellar winds. Secondly, each wind-emitting star possesses a wind reservoir that is fed from its stellar mass at a base rate:

$$\frac{\dot{M}_{\rm wind}}{\rm M_\odot\ yr^{-1}} = \min(10^{-6} L_{\rm MS}^{1.5}, 10^{-7.7} L_{\rm MS}^{2.9}) Z_{\rm star}^{0.7}, \tag{2.1.16}$$

where $L_{\rm MS}$ is the luminosity of main-sequence stars, and the metallicity $Z_{\rm star}$

is expressed in solar units. The velocity of the winds is (Lamers et al., 1995):

$$v_{\rm wind} = \sqrt{\frac{2GM_{\rm star}}{R_{\rm star}}} \times \begin{cases} 0.7 & T_{\rm eff} < 12\ 500\ {\rm K}, \\ 1.3 & 12\ 500\ {\rm K} < T_{\rm eff} < 21\ 000\ {\rm K}, \\ 2.6 & T_{\rm eff} \geq 21\ 000\ {\rm K} \end{cases} \tag{2.1.17}$$

Wolf-Rayet stars are responsible for much of the energy and momentum carried by stellar winds. Their implementation in STARFORGE is through a simple model for this phase, applied for stars above 20 $\rm M_\odot$, in which $\dot{M}_{\rm wind}$ is multiplied by a factor of 10 towards the end of their lifetime. The time a star spends in this phase is determined as:

$$T_{\rm WR} = 1.5\ {\rm Myr}\ \min\left(1, \frac{M_{\rm star}/{\rm M_\odot} - 20}{80}\right)\left(\frac{Z_{\rm star}}{Z_\odot}\right)^{0.5}. \tag{2.1.18}$$

The numerical implementation employs either local injection or cell spawning when appropriate, determined by the free-expanding radius of the winds:

$$R_{\rm free} = \sqrt{\dot{M}_{\rm wind}/v_{\rm wind}\rho}. \tag{2.1.19}$$

On the one side, if the $R_{\rm free}$ is smaller than the size of a wind cell ($\Delta x_{\rm w} = (\Delta M_{\rm w}/\rho)^{1/3}$), it is more convenient, efficient, and accurate to inject the mass, momentum, and energy isotropically into the neighbouring cells immediately. On the other side, if $R_{\rm free}$ is bigger than the size of the wind cell, then it is considered as well resolved, and the implementation switches to cell spawning, where two cells are spawned at a time using an isotropic angular distribution. Therefore, the algorithm switches adaptively between the two approaches depending on whether $R_{\rm free}$ is well resolved over at least one wind-cell length.

(iii) Supernova modelling follows a straightforward physical and numerical implementation. First, all stars more massive than 8 $\rm M_\odot$ go supernovae at the end of their lifetime, which is determined by:

$$t_{\rm star} = 9600\ {\rm Myr}\left(\frac{M_{\rm star}}{\rm M_\odot}\right)\left(\frac{L_{\rm star}}{\rm L_\odot}\right)^{-1} + 3.4\ {\rm Myr}. \tag{2.1.20}$$

At the moment a star is flagged as SN, all other forms of feedback cease, and its mass is rapidly expelled isotropically with velocity given by:

$$v_{\rm SN} = \sqrt{\frac{2E_{\rm SN}}{M_{\rm ejecta}}} = 3200 \text{ km s}^{-1} \left(\frac{E_{\rm SN}}{10^{51} \text{ erg}}\right)^{1/2} \left(\frac{M_{\rm ejecta}}{10 M_\odot}\right)^{-1/2}, \quad (2.1.21)$$

with $E_{\rm SN} = 10^{51}$ erg, and the entire star is destroyed. The numerical implementation utilises cell spawning, in which the spawned cells have the standard mass resolution $\Delta M_w = \Delta m$. These cells are spawned in shells of $N_{\rm spawn} = 24$ cells at once, continuing until all the mass from the former star is exhausted. The mass transferred from the star to the wind reservoir then proceeds at the rate given by:

$$M_{\rm SN} = \frac{N_{\rm spawn} v_{\rm SN} \Delta m}{R_{\rm sink}}. \quad (2.1.22)$$

Within the simulation, the default value is set to ≈ 1 M$_\odot$ yr^{-1} to avoid issues related to load-balance during simulations.

(iv) STARFORGE closely follows the radiation treatment developed in Hopkins et al. (2020), which tracks the emission, transport, and absorption of photons in five different wavelength bands λ. These bands are: ionising Hydrogen ($\lambda < 912$ Å), far-UV (912 Å $< \lambda <$ 1550 Å), near-UV (1550 Å $< \lambda <$ 3600 Å), near-IR (3600 Å $< \lambda <$ 3 μm), and far-IR ($\lambda >$ 3 μm). In principle, STARFOGE allows fine-tuning these bands into narrower bins to account, for instance, Lyman-Werner or He-ionising radiation, among others. In general, all sinks are treated as potential sources across all bands the aforementioned, with the emitted flux in each band calculated by treating each sink particle as black body with and effective temperature of:

$$T_{\rm eff} \approx 5780 \text{ K} (L_{\rm star}/\text{L}_\odot)^{1/4} (R_{\rm star}/\text{R}_\odot)^{-1/2}, \quad (2.1.23)$$

with $L_{\rm star}$ and $R_{\rm star}$ parameters given by the stellar evolution model within the software. Radiation from sink particles is injected into the simulation via local injection. The algorithm constructs effective oriented faces between sink particles and overlapping gas cells, $A_{\rm sg}$, and injects photons conservatively, weighted according to the solid angle subtended by each side of the face.

In the cases where the photon energy is absorbed on unresolved scales, it is re-emitted into the appropriate band by applying an extinction factor $f_{\rm abs} = \exp(-r_{\rm sg})/\lambda_{\rm mfp}$. In general, this implies that sink particles located in highly optically thick accretion regions deposit most of their luminosity into the mid- and/or far-IR bands.

2.2 Chemistry and thermodynamics

A chemical network is a collection of numerous chemical reactions of different types, such as collisional, photonic, or cosmimc-ray induced. Strictly speaking, since star formation is a long process involving almost all phases of the ISM, the number of reactions required to fully characterise each phase is extremely high. For instance, Semenov et al. (2010) build one of the largest chemical networks, which has nearly 5000 reactions, divided into gas-phase (4389) and solid-phase (532) chemistry, while also including uni-reactions with photons and CRs, designed to provide rigorous tests of state-of-the-art astrochemical codes. However, for each phase, it is possible to substantially reduce the complexity of chemical network by capturing only the most relevant reactions and key species, while also obtaining results with high fidelity and significantly reducing computational cost.

In this project, all calculations related to chemistry, heating, and cooling are handled by the thermo-chemistry library KROME (Grassi et al., 2014). KROME is capable to simplify the use of chemical networks, construct the associated ODEs, and solves it using the DLSODES solver. The physical framework by KROME to calculate the rate equations is given by Eq. (1.3.1), while the rate coefficient (k) depends on the type of reaction and its associated physical description, as stated in Eqs. (1.3.2), (1.3.3), (1.3.4). However, KROME provides a more accurate treatment of photoprocesses than Eq. (1.3.4), accounting for the molecular and energy properties of the reaction itself rather than just the extinction and environmental factors (Eq. (1.3.4)), following the methodology of Glover and Abel (2008) and Grassi et al. (2012), given by

$$R_{\rm ph} = 4\pi \int_{E_t}^{\infty} \frac{I(E)\sigma(E)}{E} e^{-\tau(E)} dE, , \tag{2.2.1}$$

where E_t is the ionisation potential of the ionised species, I(E) is the energy

distribution of the incident photon flux, $\sigma(E)$ is the cross-section of the corresponding process, $\tau(E)$ is the optical depth, and E is the photon energy.

On cooling side, KROME includes a range of cooling functions desgined for different applications:

- Atomic: This cooling accounts for interactions between electrons and both the neutral and ionised form of H and He. It considers the cooling from collisional ionisation between H, He, and He^+ by e^-; recombination of H^+, He^+, and He^{++}; collisional excitation of H (all levels), He (triplet levels 2,3, and 4), and He^+ (level n=2); as well as bremsstrahlung from all ions. All these cooling processes and their rates are taken from Cen (1992). The first of these is collisional ionisation cooling:

$$\Lambda_{\rm H} = 1.27\times10^{-21}T^{1/2}(1+T_5^{1/2})^{-1}e^{-157809.1/T}n({\rm e})n({\rm H}), \quad (2.2.2)$$

$$\Lambda_{\rm He} = 9.38\times10^{-22}T^{1/2}(1+T_5^{1/2})^{-1}e^{-285335.4/T}n({\rm e})n({\rm He}), \quad (2.2.3)$$

$$\Lambda_{\rm HeII} = 4.95\times10^{-22}T^{1/2}(1+T_5^{1/2})^{-1}e^{-631515/T}n({\rm e})n({\rm HeII}), \quad (2.2.4)$$

$$\Lambda_{\rm He\ (2\ ^3S)} = 5.01\times10^{-27}T^{-0.1687}(1+T_5^{1/2})^{-1}e^{-55338/T}n({\rm e})^2n({\rm HeII}) \quad (2.2.5)$$

Second recombination cooling:

$$\Lambda_{\rm HII} = 8.70\times10^{-27}T^{1/2}\left(\frac{T}{10^3}\right)^{-0.2}\Big/\left[1+\left(\frac{T}{10^6}\right)^{0.7}\right]n({\rm e})n({\rm HII}), \quad (2.2.6)$$

$$\Lambda_{\rm HeII} = 1.55\times10^{-26}T^{0.3647}n({\rm e})n({\rm HeII}), \quad (2.2.7)$$

$$\Lambda_{\rm HeIII} = 3.48\ \times10^{-26}T^{1/2}\left(\frac{T}{10^3}\right)^{-0.2}\Big/\left[1+\left(\frac{T}{10^6}\right)^{0.7}\right]n({\rm e})n({\rm HeIII}), \quad (2.2.8)$$

Dielectronic recombination cooling (He)

$$\Lambda_{\rm HeII} = 1.24\times10^{-13}T^{-1.5}e^{-470000/T}(1+0.3e^{-94000/T})n({\rm e})n({\rm HeIII}) \quad (2.2.9)$$

Collisional excitation cooling:

$$\Lambda_{\rm H} = 7.5 \times 10^{-19}(1+T_5^{1/2})^{-1}e^{-118348/T}n({\rm e})n({\rm H}), \tag{2.2.10}$$

$$\Lambda_{\rm HeII} = 5.54 \times 10^{-17}T^{-0.397}(1+T_5^{1/2})^{-1}e^{-473638/T}n({\rm e})n({\rm HeII}), \tag{2.2.11}$$

$$\Lambda_{\rm HeI} = 9.10 \times^{-27} T^{-0.1687}(1+T_5^{1/2})^{-1}e^{-13179/T}n({\rm e})^2n({\rm HeII}). \tag{2.2.12}$$

- Molecular hydrogen: The cooling produced by H_2 proceeds through the excitation of rovibrational states through collisions with species such as H, He, and electrons. This process is similar to a molecule 'shaking off' excess energy after being hit by nearby particles. It follows the two models presented in Galli and Palla (1998) and Glover and Abel (2008), both of which lead to the following functional form for the total gas-phase cooling by H_2:

$$\Lambda_{\rm H_2} = \frac{n_{\rm H_2}\Lambda_{\rm H2,LTE}}{1+\Lambda_{\rm H2,LTE}/\Lambda_{\rm H_2,n\longrightarrow 0}}, \tag{2.2.13}$$

where both works coincide at the high-density limit, which is expressed as

$$\Lambda_{\rm H_2,LTE} = H_R + H_V, \tag{2.2.14}$$

$$H_R = (9.5 \times 10^{-22}T_3^{3.76})/(1+0.12T_3^{2.1}) \times \exp[-(0.13/{\rm T_3})^3] + 3 \times 10^{-24}\exp[-0.51/{\rm T_3}], \tag{2.2.15}$$

$$H_V = 6.7 \times 10^{-19}\exp(-5.86/{\rm T_3}) + 1.6 \times 10^{18}\exp(-11.7/{\rm T_3}) \tag{2.2.16}$$

where H_R and H_V are the rotational and vibrational cooling, respectively, with $T_3 = T/10^3$. However, in the low-density limit, both studies diverge and lead to different expressions with temperature constraints, yielding:

$$\log(\Lambda_{\rm H_2,n\longrightarrow 0}) = n({\rm H})[-103 + 97.59\log(T) - 48.05\log(T)^2 + 10.8\log(T)^3 - 0.9032\log(T)^4]; \;\; T[{\rm K}] \in [13, 10^5], \tag{2.2.17}$$

$$\Lambda_{\rm H_2,n\longrightarrow 0} = \sum_k \Lambda_{\rm H_2,k}n_k; \;\; T[{\rm K}] \in [10, 10^4]. \tag{2.2.18}$$

In Eq. (2.2.18) (Glover and Abel, 2008) k denotes the colliding partners H and He, which are only valid within $T[{\rm K}] \in [10, 6 \times 10^3]$, and H^+ and e^- for

H_2, considered in the range $T[\mathrm{K}] \in [10, 10^4]$. Furthermore, these expressions are valid only in the optically thin limit; therefore, when the medium becomes optically thick ($n \sim 10^3$ cm^{-3}), an additional term accounting for opacity must be considered. In this regard, the model proposed by (Ripamonti and Abel, 2004) has been included to describe the cooling in the optical thick limit as

$$\Lambda_{\mathrm{H_2,thick}} = \Lambda_{\mathrm{H_2,thin}} \times \min\left[1, \left(\frac{n}{8 \times 10^9 \ \mathrm{cm^{-3}}}\right)^{-0.45}\right], \ \Lambda_{\mathrm{H_2,thin}} \equiv \Lambda_{\mathrm{H_2}} \tag{2.2.19}$$

- Collisionally induced emission: This cooling arises from the continuum emission of a photon due to the formation of a molecule with non-zero electric dipole, produced by collisions between atoms or molecules (H_2-H_2, H_2-He, H_2-H), having an important effect on high densities. Its expression has been adopted from Ripamonti and Abel (2004) as

$$\Lambda_{\mathrm{CIE,thick}} = \Lambda_{\mathrm{CIE,thin}} \times \min\left[1, \frac{1 - \mathrm{e}^{-\tau_{\mathrm{CIE}}}}{\tau_{\mathrm{CIE}}}\right], \quad \tau_{\mathrm{CIE}} = \left(\frac{n(\mathrm{H_2})}{7 \times 10^{15} \ \mathrm{cm^{-3}}}\right)^{2.8}. \tag{2.2.20}$$

Originally, Λ_{thin} was valid in the range $T[\mathrm{K}] \in [400, 7000]$. However, it is now valid for $T[\mathrm{K}] \in [100, 10^6]$, given by new fitting reported in Grassi et al. (2014):

$$\log(\Lambda_{\mathrm{CIE,thin}}) = \begin{cases} \sum_{i=0}^{5} a_i (\log T)^i, & 100 < T < 891 \ \mathrm{K} \\ \sum_{i=0}^{5} b_i (\log T)^i, & 891 \leq T < 10^5 \ K \\ c \log(T) - d, & T \geq 10^5 \mathrm{K}, \end{cases} \tag{2.2.21}$$

a_i, b_i and c coefficients are reported in Table (4) in Grassi et al. (2014).

- Chemical: In Omukai (2000), it is stated that the reactions listed in Table (5) in Grassi et al. (2014) remove energy from the gas phase in processes inherit of their reaction, thereby the jth reaction provides a cooling contribution

described as

$$\Lambda_j = E_j k_j n(R_{j1}) n(R_{j2}), \tag{2.2.22}$$

where k_j, $n(R_{j1})$, $n(R_{j2})$ represent the rate coefficient, and the number density of each reactant, respectively. The total cooling is then the total contribution of each reaction:

$$\Lambda_{\rm CHEM} = \sum_j \Lambda_j \tag{2.2.23}$$

- Metals: This type of cooling comes from fine-structure levels and the population of the species occupying them. The following metals are included in the cooling calculations: C, O, Si, Fe, C^+, O^+, Si^+, Fe^+. Each metal has different levels, transitions, and collisional partners. The total cooling contribution from metals is expressed as:

$$\Lambda_Z = \sum_{ij} n_i \Delta E_{ij} A_{ij}, \tag{2.2.24}$$

which represents the sum of energy losses in each level decay $i \longrightarrow j$ of each metal, while n_i, E_{ij}, and A_{ij} are the number density, energy loss, and Einstein coefficient, respectively.

- Compton: It consists of the compton scattering of photons originated from the cosmic microwave bakcground (CMB) by free electrons. It is parametrised by the expression presented in (Cen, 1992), which is given by:

$$\Lambda_{\rm compt} = 1.017 \times 10^{-37} T_{\rm CMB}^4 (T - T_{\rm CMB}) n_e, \tag{2.2.25}$$

where $T_{\rm CMB} = 2.73(1+z)$, and z the redshift.

- Dust: One form of cooling provided by dust is the emission of IR radiation due to the absorption of UV radiation. How KROME implements this mechanism is different than the other cooling mechanisms. Initiating and based on Hollenbach and McKee (1979), Grassi et al. (2017) developed a highly accurate fitting procedure to determine dust temperature, opacity,

and cooling from dust. According to this procedure, the dust distribution is logarithmically binned into N_d spaces, with a large number of bins to approximate a smoothly varying distribution, where the number density for the i-th distribution is then

$$n_{\mathrm{d,i}} = \mathcal{C} \int_{(a_{i-1}a_i)^{1/2}}^{(a_i a_{i+1})^{1/2}} \varphi(a)\ \mathrm{d}a, \tag{2.2.26}$$

with a the dust geometrical cross section, $\varphi(a)$ is the grain size distribution, now treated as a step function, and the integration limits correspond to the logarithmic mid-points. In the optically thin regime, the dust temperature is a quantity that can be determined for each individual bin, as dust grains can be considered separately. Therefore, the contribution from the ith dust bin to the dust cooling is then,

$$L_i = \pi a_i^2 n_{\mathrm{d,i}} k_\mathrm{B} [T_g - T_{d,i}], \tag{2.2.27}$$

with k_B, T_g and T_d being the Boltzmann constant, gas and dust temperature, respectively. Finally, the previous equation can be integrated over the bin distribution to find the total gas cooling:

$$\Lambda = 2 f v_g n_\mathrm{tot} \sum_{i=1}^{N_\mathrm{d}} L_i \tag{2.2.28}$$

,

with f accounting for gas–grain collisions with atoms and molecules other than H, such as He and charged species, v_g is the thermal velocity of the gas, and n_tot is the total number density.

- Bremsstrahlung: It arises when free electrons emit a photon as they accelerate or decelerate while passing near the electric field created by charged ions. KROME implements this mechanism following Cen (1992):

$$\Lambda_\mathrm{Bremss} = 1.42 \times 10^{-27} g_\mathrm{ff} T^{1/2} \left[\sum_j n(X_j) \right], \tag{2.2.29}$$

with g_ff as the mean gaunt factor value and the sum over all ionised species

X_j.

The total heating in KROME has been divided in several components listed below along with their descriptions:

- Chemical: This heating function considers H_2 formation in the gas phase. Following Omukai (2000), the total heating of this process is given by.

$$\Gamma_{\rm chem} = \Gamma_{\rm H_2,3b} + \Gamma_{\rm H^-} + \Gamma_{\rm H_2^+}, \tag{2.2.30}$$

where each term on the right-hand side represents the total energy deposited as heating by each reaction forming H_2. In the order given, each term corresponds to the following reaction:

$$\begin{aligned} \rm H + H + H &\longrightarrow H_2 + H \\ \rm H^- + H &\longrightarrow H_2 + e^- \\ \rm H_2^+ + H &\longrightarrow H_2 + H^+ \end{aligned}$$

Each term is expressed as following:

$$\Gamma_{\rm H_2,3b} = 4.48 f k_{\rm H_2,3b} n_H^3, \tag{2.2.31}$$
$$\Gamma_{\rm H^-} = 3.53 f k_{\rm H^-} n_{\rm H} n_{\rm H^-}, \tag{2.2.32}$$
$$\Gamma_{\rm H_2^+} = 1.83 f k_{\rm H_2^+} n_{\rm H} n_{\rm H_2^+}, \tag{2.2.33}$$

with k_i the rate coefficient. Analogously, H_2 formation over dust grains also contributes to the total heating, which is expressed as:

$$\Gamma_{\rm H_2dust} = k_d(0.2 + 4.2f) n_{\rm H} n_{\rm d}, \tag{2.2.34}$$

where n_d and k_d correspond to the formation on the grain surface and the dust number density, respectively. The f parameter in Eqs. (2.2.31)-(2.2.34) represents the heat deposited per molecular hydrogen formed, weighted by

a critical density factor (Hollenbach and McKee, 1979):

$$f = \left(1 + \frac{n_{\rm cr}}{n_{\rm tot}}\right)^{-1}, \tag{2.2.35}$$

and $n_{\rm cr}$ defined as

$$n_{\rm cr} = 10^6 T^{-1/2} \left\{ 1.6 n_{\rm H} \exp\left[-\left(\frac{400}{T}\right)^2 \right] + 1.4 n_{\rm H_2} \exp\left[-\frac{12000}{T + 12000} \right] \right\} \tag{2.2.36}$$

- Photoheating: This heating mechanism occurs when a photoionisation event releases an e^- into the gas phase, carrying the energy transferred from the incident photon and thereby thermalising the gas. Analogously to Eq. (2.2.1), the total heating is given by:

$$\Gamma_{\rm ph} = n_X \left[4\pi \int_{E_t}^{\infty} \frac{I(E)\sigma(E)}{E} e^{-\tau(E)} (E - E_t) \eta(E) \, {\rm dE} \right], \tag{2.2.37}$$

  where the parameters in the square brackets are the same as in Eq. (2.2.1), with E_t and $\eta(E)$ representing the ionisation energy of the species and the efficiency factor accounting for the amount of energy released into the gas-phase, respectively, while n_X is the number density of the ionised specie.

- Cosmic ray heating: This accounts for the heating deposited into the gas during the collisional ionisation. The formulation follows Galli and Padovani (2015), parametrising the CR heating as

$$\Gamma_{\rm CR} = Q({\rm H}) n({\rm H}) k_{\rm H} + Q({\rm He}) n({\rm He}) k_{\rm He} + Q({\rm H_2}) n({\rm H_2}) k_{\rm H_2} + \sum_j Q_{\rm c} n(R_j) k_j, \tag{2.2.38}$$

  where Q represents the heating produced when a CR ionises the species at the argument, k_j denotes the rate coefficient of the CR reaction, and n is the number density of the reactant. The first two terms account for the heat deposited into the gas when CRs ionise H and He respectively. Glassgold et al. (2012) reported that the heating generated from these two reactions under

MC conditions corresponds to 4.3 eV, implying $Q(\mathrm{H}) = Q(\mathrm{He}) = 4.3$ eV. The third term is analogous for H_2, but the determination of Q is fitted following Galli and Padovani (2015) and expressed in Eq. (2.2.39) with the γ_i coefficients tabulated in Table (2.2.1). The sum in the fourth term follows the parametrisation as the previous three terms but is generalised for all other CR reactions and reactants, with each depositing $Q_c = 20$ eV as heating into the gas phase.

$$Q(\mathrm{H_2}) = \begin{cases} 1, & n(\mathrm{H_2}) < \omega_1, \\ \gamma_1 \log(n(\mathrm{H_2})) + \gamma_2, & \omega_1 \leq n(\mathrm{H_2}) < 10^5, \\ \gamma_3, & n(\mathrm{H_2}) > 10^{10}, \\ \gamma_4 + \sum_{i=1}^{4} (-1)^i \gamma_{4+i} \log(n(\mathrm{H_2}))^i, & \text{otherwise.} \end{cases} \tag{2.2.39}$$

	coefficients
γ_1	1.4510849135088
γ_2	7.23277032061136
γ_3	18.021719523307954
γ_4	9.1462198642562
γ_5	0.443120145068494
γ_6	0.601271617560071
γ_7	0.0710284101055109
γ_8	0.00242079494592405
ω_1	$1.0366017494884676 \times 10^{-5}$

Table 2.2.1: Coefficients for Eq. (2.2.39).

- Photo-electric heating: It accounts for the heating produced when dust grains absorb UV radiation, resulting in the ejection of electrons. KROME handles both the heating and cooling generated by this process. On one hand, the ejected electron heats the gas through collisions, transferring its kinetic energy. On the other hand, cooling occurs via recombination between the ejected electron and the positively charged dust grain, which is relevant when the energy of the ejected electron is lower than the thermal energy of the electron recombining on the dust grain. Therefore, the net heating is

obtained by subtracting these two competing mechanisms:

$$\Gamma_{\text{photoelectric}} = \Gamma_{\text{ejec}} - \Lambda_{\text{reco}}. \tag{2.2.40}$$

The formula includes the heating and cooling terms due to the ejected electrons, corresponding respectively to the energy transferred to the gas through collisions and the recombination between the ejected electrons and positively charged dust grains. The expression for the heating term is based on Bakes and Tielens (1994), with the rate approximated as:

$$\Gamma_{\text{ejec}} = 10^{-24}\epsilon G_0 n_{\text{H}} \tag{2.2.41}$$

$$\epsilon = \frac{4.87 \times 10^{-2}}{1 + 4 \times 10^{-3}(G_0 T^{1/2}/n_{\text{e}})^{0.73}} + \frac{3.65 \times 10^{-2}(T/10^4)^{0.7}}{1 + 2 \times 10^{-4}(G_0 T^{1/2}/n_{\text{e}})}, \tag{2.2.42}$$

with the gas temperature T, the intensity of the incident far-UV field in units of the Habing interstellar radiation field, G_0, and the electron number density n_{e}. Analogously, the expression for the cooling term is based on Wolfire et al. (1995), rate approximated as:

$$\Lambda_{\text{reco}} = 4.65 \times 10^{-30} T^{0.94} (G_0 T^{1/2}/n_{\text{e}})^{\beta} n_{\text{e}} n_{\text{H}}, \tag{2.2.43}$$

$$\beta = \frac{0.74}{T^{0.068}}, \tag{2.2.44}$$

with n_{H} being the H number density.

Finally, the temperature evolution of the environment is determined by the total contributions from both heating and cooling, expressed as

$$\frac{\text{dT}}{\text{dt}} = (\gamma - 1)\frac{\Gamma(T, \bar{n}) - \Lambda(T, \bar{n})}{k_b \sum_i n_i}, \tag{2.2.45}$$

where $\bar{n}$ and k_b are the vectors containing the abundances of all species and the Boltzmann constant, respectively. The sum represents the weighting of the total gas number density, while γ is the adiabatic index, defined as in Grassi et al. (2011)

$$\gamma = \frac{5n_{\text{H}} + 5n_{\text{He}} + 5n_{\text{e}} + 7n_{\text{H}_2}}{3n_{\text{H}} + 3n_{\text{He}} + 3n_{\text{e}} + 5n_{\text{H}_2}}, \tag{2.2.46}$$

where each subscript denotes the species required for the number densities.

Chapter 3

Methodology

3.0.1 Cosmic-ray propagation scheme

3.0.1.1 Numerical framework

In many studies CRs are strongly simplified in order to include their presence while reducing the computational cost associated with modelling them accurately. A typical approach is to set $\zeta = 10^{-17}$ s^{-1} as a constant "flux", neglecting energy losses and consistent propagation. On the other hand, several studies have attempted to determine the CR ionisation rate from observational tracers, including high-mass star-forming regions (Sabatini et al., 2020, 2023), circumstellar discs (Ceccarelli et al., 2014) and low-mass dense cores (Caselli et al., 1998; Redaelli et al., 2021; Bialy, Shmuel et al., 2022). More recently, few studies have attempted to couple CRs with MHD simulations (Chan et al., 2019; Winner et al., 2019; Bustard and Zweibel, 2021; Ogrodnik et al., 2021; Thomas et al., 2021) but with different limitations. For this reason, in this work it is introduced a numerical approach to account CR propagation and attenuation in magnetised cloud simulations in post-processing.

The propagation scheme consists of mimicking the continuous CRs flux with each CRs modelled as tracer particles (TPs) that propagate throug the medium. As CRs are charged particles, the simulated medium (here, MCs) must include magnetic fields for the CRs to propagate following their line paths. At each step of their propagation, CRs lose energy through collisions with the gas, resulting in an effective attenuation of the flux deeper within the cloud at increasingly high

densities.

The structure of the algorithm is as follows:

(i) A specific number of CRs are created following 2^p at a distance R from the cloud and randomly distributed over a spherical surface centred on the cloud, with their initial direction point towards the centre of the cloud, and all are assumed to originate from an uniform isotropic distribution of pitch angles α_0 over a hemisphere. The pitch angle distribution ranges from 0 to $\pi/2$, sampled using N_α bins. At each initial value of the pitch angle distribution, TPs are assigned an initial column density defined as

$$N_{\rm eff}(x_0, \alpha_0) = \frac{2 \times 10^{21}\ {\rm cm}^{-2}}{\cos \alpha_0}, \tag{3.0.1}$$

where $N_{\rm eff}$ stands for the effective column density traversed by TPs, and 2×10^{21} cm^{-2} is the column density value at which hydrogen is mainly in its molecular form (Snow and McCall, 2006).

(ii) At each step of a tracer particle's motion, the column density traversed is computed. To do this, the local properties of the gas, $n(\mathrm{H_2})$ and the mean magnetic field, are required, where both quantities are estimated using the kernel weighting. Specifically, at the location x_k of the k-th TP, the kernel size h_k is determined for encompassing an effective number of gas-neighbours $N_{\rm ngb} = 32$, defined by

$$N_{\rm ngb} = \frac{4\pi}{3} h_k^3 \sum_j W(x_j - x_k, h_k), \tag{3.0.2}$$

where the sum is over all neighbours within h_k, the location of the j-th neighbour is x_j, and the kernel function $W(x_j - x_k, h_k)$ is defined by the standard cubic spline:

$$\bar{W}(q, h_k) = \frac{8}{\pi h_k^3} \begin{cases} 1 - 6q^2 + 6q^3, & 0 \leq 1 \leq \frac{1}{2}, \\ 2(1-q)^3, & \frac{1}{2} < q \leq 1, \\ 0, & q > 1, \end{cases} \tag{3.0.3}$$

with $q = |x_j - x_k|/h_k$ being the normalised distance. The neighbour search

represents the most computationally expensive part of the algorithm, as it must be repeated at every integration step for all tracer particles. To limit the computational cost, the algorithm performs the search using a Newton-Raphson iteration (Hopkins, 2015). After the search converged to 32 gas-neighbours, a last loop is performed to compute the smoothed magnetic field and gas density to ultimately update the column density.

(iii) The propagation of TPs is computed using the fourth-order Runge-Kutta integrator, where the step side for the k-th TP is calculated as $\Delta\ell_k = 0.1\Delta x_k$, with $\Delta x_k = (4\pi/3)^{1/3} N_{ngb}^{-1/3} h_k$ being the grid-equivalent inter-particle spacing. The motion occurs along the direction of the smoothed magnetic field.

(iv) After TPs have moved, the column densities and CR ionisation rate must be updated. Therefore, the new position x' and the new interpolated quantities $n(x')$ and $B(x')$ are then used to compute the expression

$$N_{\rm eff}(x', \alpha_0) = N_{\rm eff}(x, \alpha_0) + \frac{n(x')\Delta\ell_k}{\sqrt{1 - B_k(x')\sin^2(\alpha_0)/B_{k,0}}}. \tag{3.0.4}$$

Subsequently, the CR ionisation rate is re-estimated by integrating, using the trapezoidal rule, over all the pitch angles as

$$\zeta_2 = \delta(x') \int_0^{\pi/2} f[N_{\rm eff}(x', \alpha)] \sin\alpha \, {\rm d}\alpha, \tag{3.0.5}$$

where $\delta(x') = B(x')/B_0$ accounts for the increase in ζ_2 due to the growth in the magnetic flux, with $B(x')$ the magnetic field at the current position and B_0 the field at the TP injection, $\sin\alpha$ accounts for the spherical distribution of the pitch angles (analogously to Eq. (6) in Padovani et al. (2013)) at the TP injection, and f converts $N_{\rm eff}$ into the corresponding ζ_2 according to the relations presented in Fig. (F.1) of Padovani et al. (2018), where three curves represent different levels of ζ_2 and account for the H_2 ionisation by protons and primary and secondary electrons. We considered model $\mathscr{H}$ and $\mathscr{L}$, which represent the average cosmic-ray ionisation rate on diffuse media and data obtained from the two Voyager spacecraft. In the algorithm, the argument of the square root in Eq. (3.0.4) could become negative or equal to

zero, which physically corresponds to the particles being mirrored backwards (Silsbee et al., 2018). To avoid this, it is defined $B_{\rm crit} = B_0/\sin^2(\alpha_0)$ as an upper limit for non-mirroring particles, the propagation scheme then includes this effect by assuming that the reflected particles above $B_{\rm crit}$ are neglected in the evaluation of Eq. (3.0.5).

(v) At the end of each iteration of the algorithm, the computed ζ_2 value of each TP is deposited on each gas particle that contributed for its calculation, weighted by the smoothing kernel. Since the same gas particle can contribute for the ζ_2 calculation at different iterations, the final ζ_2 determination for each gas particle is computed only at the end of the entire procedure following:

$$\zeta_2^j = \frac{\sum_{k=1}^{Np} W(x_j - x_k, h_k)\zeta_2(x_k)}{\sum_{k=1}^{N_p} W(x_j - x_k, h_k)}. \tag{3.0.6}$$

In the algorithm, steps (ii)-(iv) are repeated over all active TPs, with a TP considered active until one of the following two conditions is satisfied: (a) the CR flux becomes negligible, which occurs once the effective column density reaches $N_{\rm eff} > 10^{29}$ cm^{-2}, or (b) TPs leave the spherical region around the cloud, defined by an outer boundary spherical surface, located at $R_{\rm out} = 1.02\,\max_j\{r_j\}$, with r_j the distance of the jth gas particle from the centre of the cloud. The algorithm finishes once all TPs become inactive, that is, they completed their propagation throughout the cloud.

The final output of the propagation scheme, of which an schematic illustration of the entire process is displayed in Fig. (3.0.1), is a 3D distribution of ζ_2 generated from the magnetised cloud at a specific time. If the algorithm is applied at each time step of the simulation, it is possible to track the time evolution of ζ_2 as the gas evolves.

3.0.1.2 Chemistry in post-processing

The output of the algorithm can be used to chemically evolve the cloud with time-dependent chemistry over the time-scale of the simulation. Since the chemical evolution is performed in post-processing, coupling the cloud dynamics with the chemical evolution while accounting for the ζ_2 values from the propagation scheme is achieved using the tool developed by Ferrada-Chamorro et al. (2021), which

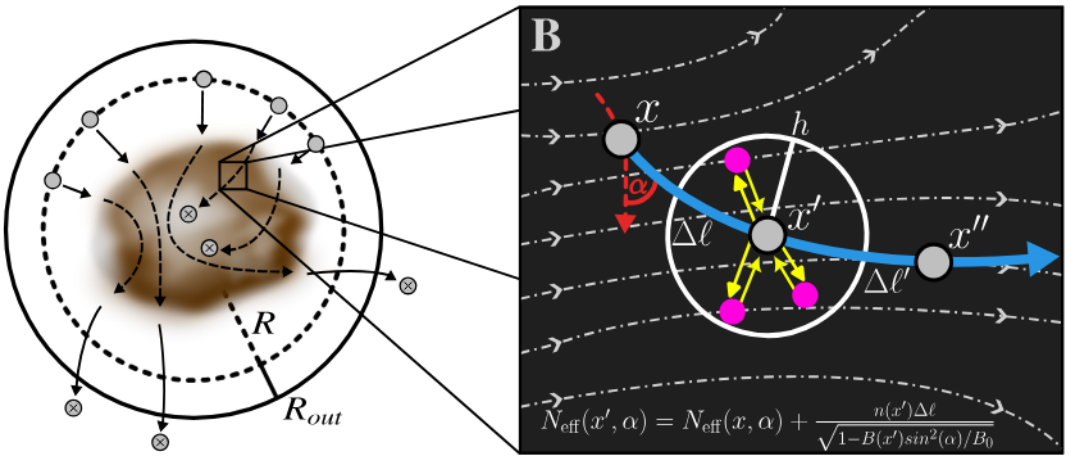

Figure 3.0.1: Sketch of the CR propagation scheme. The left panel describes the TP propagation through the domain. TPs (grey dots) are created from a spherical surface of radius R (dashed black circle) with radial inward trajectories (step i). TPs are then deactivated when the column density that is traversed exceeds 10^{29} cm^{-2} or when they leave the outer spherical surface at a distance $R_{\rm out}$ (solid black circle) as shown by the crossed grey dots. The right panel instead highlights the propagation of a single TP. The trajectory is shown by the curved solid blue arrow, and the magnetic field lines (B) are reported as dash-dotted grey lines. The pitch angle (α) between the TP velocity and the local magnetic field is shown as the dashed red line. The displacement of the TP between the previous (x) and the current (x') location is defined by the step size $\Delta\ell$ (step iii). To compute the effective column density of the TP, the average local density ($n(x')$) and local magnetic field ($B(x')$) were estimated from gas particles (pink dots) within the kernel size h (thin yellow arrows; step ii). Then, its value was used to update the CR ionisation rate (ζ_2; step iv), which was finally deposited at the location of the original gas particle (thick yellow arrows; step v).

implements the thermo-chemistry library KROME (Grassi et al., 2014).

The magnetised cloud simulation selected to test the CR propagation algorithm was the simulation conducted in Bovino et al. (2019), particularly the "M1" case, which represents a slow core collapse. This case was chosen over the others (M0, M2, M3) because the slow collapse provides a longer timeframe in which the impact of the CR ionisation rate is relevant, allowing a more detailed study of its evolution before the first stars form. The other faster-collapse cases would form stars too quickly to examine the effect exhaustively. Additionally, the simulations performed include a chemical network with 143 species and 4616 reactions, including the ortho-para branch of H_2 and H_3^+, and is strongly focused on deuterium (D) for the assessment of CO depletion and the resulting deuteration.

To assess the non-linear ζ_2 impact on the chemistry, CR propagation was simulated using the $\mathscr{H}$ and $\mathscr{L}$ energy spectra modelled by Padovani et al. (2018), and an additional third case was considered symbolised by $\mathscr{C}$, defined as $\zeta_2 = 2.5 \times 10^{-17}$ s^{-1}, equivalent to the original value set in Bovino et al. (2019). Then, the key species HCO^+, N_2H^+, DCO^+, N_2D^+, and o-H_2D^+ will be examine, as they are strongly sensitive to variations in ζ_2.

3.0.2 Chemical network

Once the coupling has been completed, the next step is to build the proper chemical network. Since the goal is to simulate a GMC from its origin to dispersion, including all stellar feedback, the network must account for gas- and solid-phase chemistry, as well as uni-reactions such as those induced by CRs and radiation. The network is based on Lupi et al. (2021), which is an updated version of Glover et al. (2010) and subsequently Grassi et al. (2017). To accurately describe photo-dissociation and photo-ionisation, the original Draine-based rate coefficients (Eq. (1.3.4)) are now replaced with the bin-approach formula of Eq. (2.2.1), which requires cross-section (σ) data for the species instead of the visual extinction (A_v). The Leiden database (Heays et al., 2017) and the Southwest Research Institute (SWRI) provide the experimental cross sections in order to satisfy the formula for most of the uni-reactions, while for those reactions with no data are neglected in the network. The original network contained 40 species, which now has been expanded to include nitrogen chemistry and solid-phase reactions, Nitrogen-bearing species were taken from standard networks, while surface chemistry includes carbon hydrogenation up to methanol (CH_3OH), along with two-body surface reactions. The final species list includes: H, H^+, He, He^+, He^{++}, o/p-H_2, o/p-H_2^+, o/p-H_3^+,H^-, C^+, C, O^+, O, OH, HOC^+, HCO+, CO, CH, CH_2, C_2, HCO, H_2O, O_2, CH^+, CH_2^+, CO^+, CH_3^+, OH^+, H_2O^+, H_3O^+, O_2^+, C^-, O^-, e^- (electrons), and dust grains GRAIN0, GRAIN−, and GRAIN+. New included species are: Si, Si^+, Si^{++}, N, N_2, NO, CN, N^+, NH, NH^+, NH_2, NH_2^+, NH_3, NH_3^+, NH_4^+, N_2H^+, HCN, HCN^+, HNC, $HCNH^+$, totalling 60 species and connected by 638 reactions. The formation of H_2 on dust has also been included considering OPR = 3 at formation, along with adsorption, desorption, and two-body surface reactions for species such as: H, C, O, CO, CO_2, H_2O, OH, O_2, HO_2, HCO, H_2CO, CH_3O, CH_3OH, H_2O_2, O_3, CH, CH_2, CH_3, N, N_2, NH, NH_2, NH_3, CN, HCN, NO, HNC. Additional processes incude ortho-para

conversion via collisions with H^+ and H_3^+, ionisation and dissociation induced by CRs, electron attachment, and recombination of positive ions on dust grains.

On one hand, the rate coefficients associated to the gas-phase reactions are mostly described using the formula Eq. (1.3.2), with ion-neutrals reaction described through Eq. (1.3.5),(1.3.6) when the α, β, and γ coefficients are not available. On the other hand, the rate coefficients associated to the solid-phase reactions are implemented in KROME following the physical framework of Semenov et al. (2010), which accounts for:

- adsorption to dust grain:

$$R_{\rm acc}(i) = k_{\rm acc}(i) n(i), \tag{3.0.7}$$

  where $n(i)$ is the density of gas-phase species i ($\rm cm^{-3}$), and $k_{\rm acc}(i) = \sigma_{\rm d} \langle v(i) \rangle n_{\rm d}$ is the accretion rate, with $\sigma_{\rm d} = \pi a_{\rm g}^2$ as the geometrical cross section of the grain of radius $a_{\rm g}$, the dust density $n_{\rm d}$, and the thermal velocity $\langle v(i) \rangle = \sqrt{8 k_{\rm B} T / (\pi \mu(i) m_{\rm p})}$, with T as gas temperature (K), $m_{\rm p}$ being the proton mass, $\mu(i)$ the reduced mass of the molecule, and the Boltzmann constant $k_{\rm b}$.

- thermal desorption for warm medium determined by the Polanyi-Wigner equation:

$$k_{\rm des}(T_{\rm d}) = \nu(i) \exp\left(- \frac{E_{\rm des}}{T_{\rm d}} \right), \quad \nu(i) = \sqrt{\frac{2 N_{\rm s} k_{\rm B} E_{\rm des}}{\pi^2 m m_{\rm p}}}, \tag{3.0.8}$$

  where $\nu(i)$ is the characteristic vibrational frequency of the ith species, $E_{\rm des}$ (Garrod and Herbst, 2006) its desorption energy (K), m the mass of the species, and $T_{\rm d}$ the grain temperature.

- desorption by CRs collisions:

$$k_{\rm crd} = f k_{\rm des}(70 \text{ K}), \tag{3.0.9}$$

  with f represents the fraction of energy retained by the dust grain, defined as the ratio of the grain cooling timescale via molecular desorption to the timescale of subsequent heating events. This expression is based on the

assumption that a cosmic-ray particle (typically an iron nucleus) deposits on average 0.4 MeV into a dust grain of the adopted radius, impulsively raising its temperature to a peak value of $T_{\rm crp} = 70$ K (Hasegawa and Umemura, 1993).

- The rate coefficients between species i and j in surface reactions are described as

$$k_{i,j} = P(R_{\rm diff}(i) + R_{\rm diff}(j))/n_{\rm d}, \tag{3.0.10}$$

where P is the probability for the reaction to occur and accounts for the tunnelling effect (Hasegawa et al., 1992):

$$P = \alpha \exp[-2(b/\hbar)(2k_{\rm B}\mu(i)m_{\rm p}E_a)^{1/2}], \tag{3.0.11}$$

with b the barrier thickness, $\hbar$ is the Planck constant multiplied by 2π, and $R_{\rm diff}$ is the diffusion rate of the species i as:

$$R_{\rm diff}(i) = \nu(i) \exp\left(- \frac{T_{\rm diff}(i)}{T_{\rm d}} \right)/S, \tag{3.0.12}$$

with $T_{\rm diff}$ as the activation energy of diffusion for the ith molecule and S the total number of sites (or cavities) per grain.

This network, as in Bovino et al. (2019), includes the updated rate coefficients carried out by several studies (Oka, 2004; Pagani et al., 2009; Sipilä et al., 2015) to account for spin-state reactions between branched (o/p-H_2 and o/p-H_3^+) and non-branched species (H, OH, N_2), while the majority of the other reactions use rate coefficients from KIDA (KInematic Database for Astrochemistry; Wakelam et al., 2012).

Once the network is completed, it is subjected to a few tests performed with KROME in order to examine the abundance evolution of key species, which serve to evaluate the whole network and thermal evolution with varying densities. The first set of tests aims to compare the resulting abundance profiles of these key species (representative of the entire network) with the large network developed by Semenov et al. (2010), under the MC conditions where adsorption ($T = 10$ K)

and desorption ($T \geq 70$ K; Leger et al., 1985) are efficient. The second set of tests is performed under one-zoned cloud collapse conditions, aimed to evaluate the thermal evolution under varying density and considering several cooling and heating mechanisms. Specifically, these results were compared against the results in Omukai (2000) for validation. Finally, the chemical network was employed in a numerical simulation for a GMC performed with STARFORGE coupled with KROME, enabling the simultaneous computation of detailed microphysical processes.

Chapter 4

Results

4.0.1 CR propagation framework

4.0.1.1 Convergence and relative errors of the algorithm

Accurately covering and tracing the entire cloud requires the use of a high number of TPs. However, doing so would be computationally expensive, since searching for the appropriate kernel length h to ensure $N_{\rm ngb} = 32$ represents the main source of overhead. Therefore, increasing the number of TPs by factors of two would approximately double the computational time. To evaluate this, a series of runs with different numbers of TPs were performed in order to determine the appropriate number that neither substantially increases the computational time nor significantly decreases the accuracy of the ζ_2 distribution, as indicated in Table (4.0.1).

ID	X1	**X2**	X4	X8	X16	X32
#TP	5120	**10240**	20480	40960	81920	163840

Table 4.0.1: Number of TPs used in the series of runs performed. The fiducial case is highlighted in boldface.

Fig. (4.0.1) shows the ζ_2 distribution per gas particle for $\mathscr{H}$ and $\mathscr{L}$ models. The fiducial case corresponds to the minimum number of TPs required for convergence, that is, **X2** case, depicted as pink. The shape of the distribution is reasonable well preserved throughout all runs, since the physical properties of the cloud that determine the distribution are unchanged. Most of the gas particles with high ζ_2

values are concentrated on the rightmost side of the distribution, corresponding to TPs located near the edge of the cloud, where attenuation is not strong yet. The steep decrease towards the left reflects the increasing attenuation as TPs traverse the dense central regions of the cloud. The observed differences can be attributed to the TP number used, which affects the smoothing procedure and integration step. In both models, the X1 case exhibits an excess at the edges of the distribution due to poor spatial sampling, which is more sensitive to outliers. Increasing the number of TPs improves spatial sampling at the edges of the cloud (the rightmost edge of the distribution), but does not change the low-ζ_2 tail, which shows stochastic variations due to the small number of gas particles in the central region.

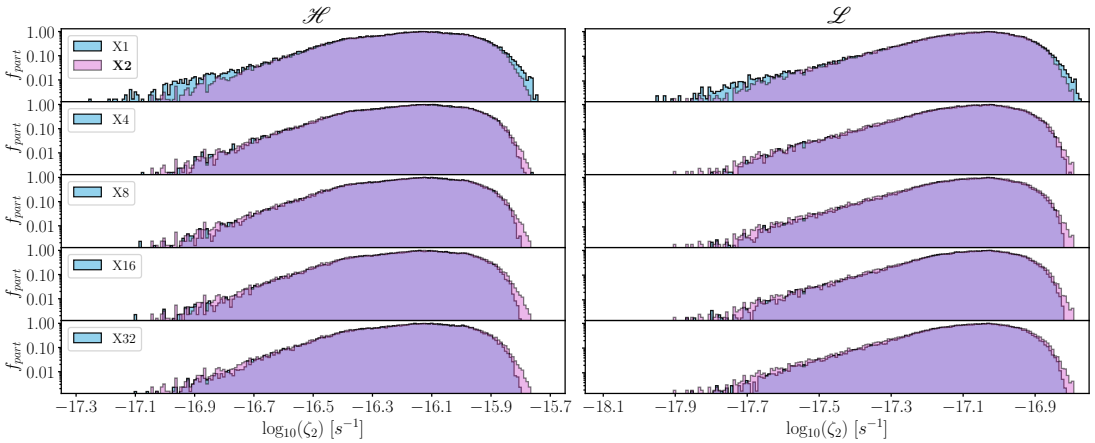

Figure 4.0.1: ζ_2 distribution $\mathscr{H}$ (left) and $\mathscr{L}$ (right) at 153.3 kyr in a $0.2 \times 0.2 \times 0.2$ pc^{-3} box. In each row, we compared one of the runs showed in Table (4.0.1) (in cyan) with our fiducial case (X2, in pink), with the matching regions in purple. $f_{\rm part}$ represents the fraction of particles.

Similarly, Fig.(4.0.2) shows the relative difference between ζ_2 obtained in the fiducial case (X2), and the other runs from Table (4.0.1), averaged along a LOS aligned with z-axis. The largest and smallest relative error among the pixels are indicated in the bottom-left corner of every panel, corresponding to X1, X4, X8, X16, and X32 from top to bottom. It is noticeable that, due to the poor spatial sampling, the X1 case exhibits the largest deviations, while the other runs oscillate around 10-20%, almost independently of resolution. Moreover, to check the robustness of the distributions, the relative error was determined within a spherical region of radius 0.065 pc (similar to the filament size). In this case, the

error is almost halved, reaching at most 3-13% for both models. Therefore, the use of 10.240 TPs is adequate as our base for further runs.

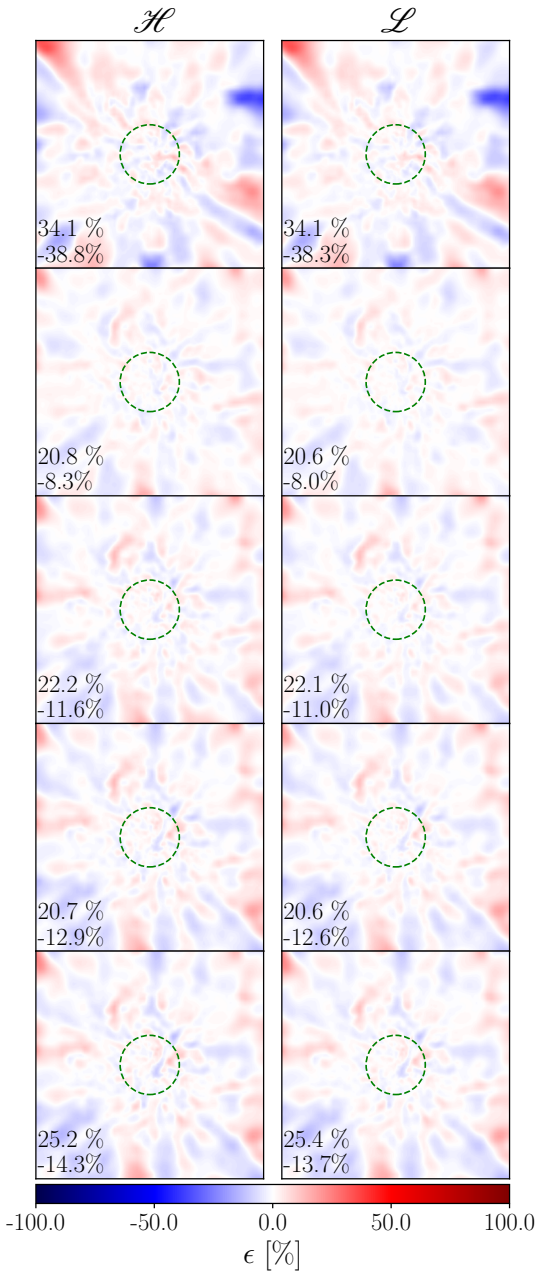

Figure 4.0.2: Relative error (ϵ) for $\mathscr{H}$ and $\mathscr{L}$ within a $0.5 \times 0.5 \times 0.2$ pc^3 at 153.3 kyr. The box size takes into account the 0.5pc injection and a depth length similar to the filament scale (0.2 pc) to avoid the inclusion of background particles. The errors are calculated between X2 case and the rest. The panels are, from top to bottom: X1, X4, X8, X16 and X32. The bluer and redder indicate underestimation and overestimation of X2 relative to the ther. The maximum and minimum errors for each comparison are written in the bottom-left corner. All green spheres have 0.065 pc radii.

4.0.1.2 Distribution of the cosmic-ray ionisation rate

The propagation scheme was applied to the magnetised cloud simulated in Bovino et al. (2019). The resulting 3D distribution of the density-weighted ζ_2 ($\mathscr{H}$ and $\mathscr{L}$) is shown in Fig.(4.0.3) for three different time steps, with green arrows overplotted corresponding to the x-y projection of the MF lines. The ζ_2 differs by approximately one order of magnitude between the two models, while the attenuation spans approximately 0.6 dex regardless of the initial energy at injection. The figure highlights the region of strongest attenuation, being $10^{-16.2}$ s^{-1} ($\mathscr{H}$) and $10^{-17.1}$ s^{-1} ($\mathscr{L}$), which coincides with the highly bent and twisted lines and covers (and identifies) the cloud's high-density region. This complex line pattern results in a substantial increase in the effective column density traversed by CRs, enhancing the attenuation. In contrast, the high-ζ_2 values are found in the background region, where CRs are almost unattenuated.

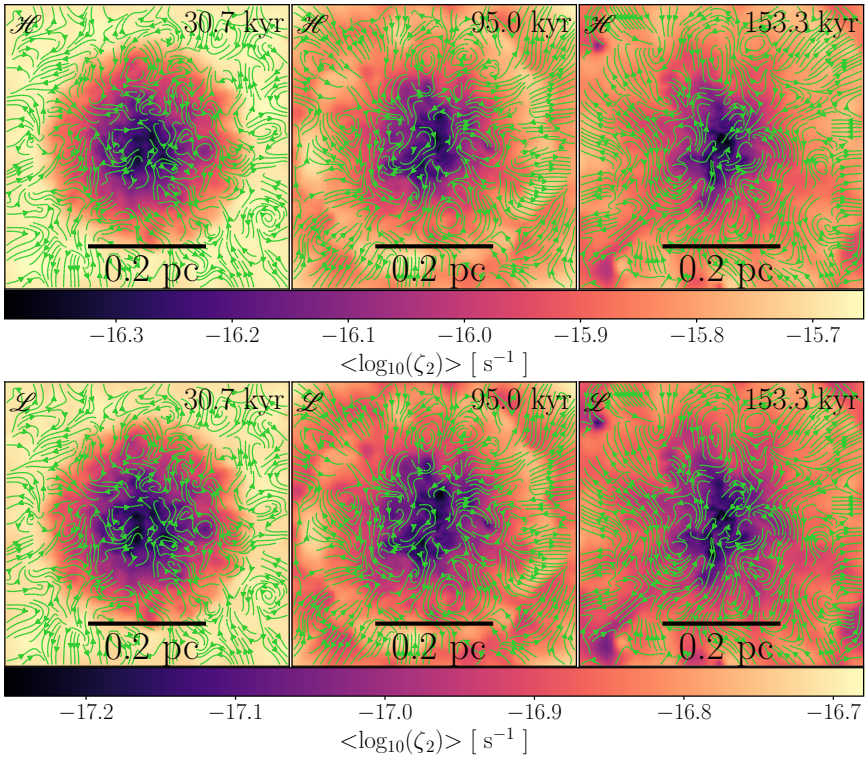

Figure 4.0.3: Time evolution of the density-weighted for models $\mathscr{H}$ (top panels) and $\mathscr{L}$ (bottom panels) in a sphere of 0.5 pc radius, inside which CRs are propagated. The green arrows correspond to the x-y projection of the magnetic field lines. The two different models yield a difference of one order of magnitude within the high-density region.

The time evolution of the CR ionisation rate distribution for the two models within a $0.2 \times 0.2 \times 0.2$ pc^3 box centred at the peak of the high-density region is shown in Fig. (4.0.4). Both distributions indicate that, regardless of the initial ζ_2 computed at injection, the attenuation reduces the initial ionisation rate by more than one order of magnitude. The distribution remain mostly unchanged over time in the intervals $10^{-16.4}$ to $10^{-15.8}$ s^{-1} ($\mathscr{H}$) and $10^{-17.3}$ to $10^{-16.7}$ ($\mathscr{L}$), except at the low- and high-end tails. In particular, the low-ζ_2 tail, that is related to the innermost region of the cloud totalling approximately 1% of the total mass, fluctuates over time without a clear evolutionary trend. Comparing the lowest ionisation rates per distribution, $\sim 10^{-17.1}$ ($\mathscr{H}$) and $\sim 10^{-18}$ s^{-1}, with Fig. (F.1) of Padovani et al. (2018), these ionisation rate values correspond to column densities of $\sim 10^{25-26}$ cm^{-2}. However, this effect arises from the pitch angles that were not considered in Eq. (3.0.5) due to the mirroring effect, rather than from a high column density accumulated by the TPs.

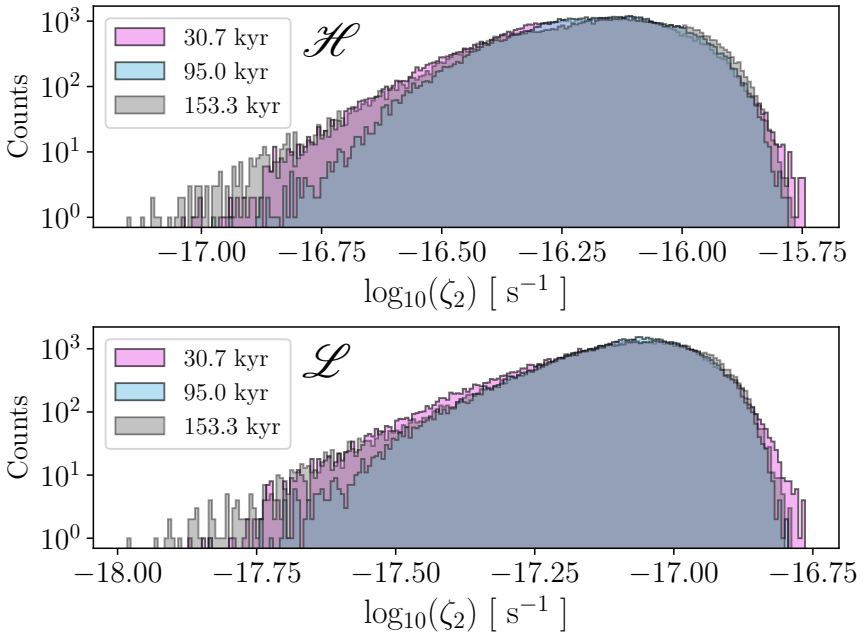

Figure 4.0.4: Time evolution of the distribution of ζ_2 for gas particles in the simulation for models $\mathscr{H}$ (top) and $\mathscr{L}$ (bottom). The distributions are determined from a box of $0.2 \times 0.2 \times 0.2$ pc^3, which only includes particles from the simulated cloud, i.e., with identical mass. The rightmost edge of the distribution shrinks over time as the gas particles within the box become denser. The low-end tail of the distribution expands towards lower ionisation rates, which is consistent with the evolution of the gas density.

4.0.1.3 ζ_2 dependence on local properties

Because the propagation of CRs in numerical simulations is computationally expensive, it is common to find articles with models that relate gas density to ζ_2 (Gaches et al., 2022). However, the present numerical framework provides the ability to determine more accurate semi-analytic prescriptions and to examine how these prescription might depend on the CR model considered. In Fig. (4.0.1.3), the correlation between CR ionisation rate and the number density of H_2, with the viridis and magma histograms as $\mathscr{H}$ and $\mathscr{L}$ models, respectively, is shown. The trend, which is negative in both models, was fitted with power laws and depicted as solid ($\mathscr{H}$) and dashed ($\mathscr{L}$) lines, given by the following expressions:

$$\log_{10}\zeta_2^{\mathscr{H}} = -0.22\log_{10} n(\mathrm{H_2}) - 15.06, \tag{4.0.1}$$

$$\log_{10}\zeta_2^{\mathscr{L}} = -0.12\log_{10} n(\mathrm{H_2}) - 16.45. \tag{4.0.2}$$

The 3D structure of the system affects the different LOS, producing a slightly different CR ionisation rate, with a scatter of $\sigma^{\mathscr{H}} = 0.25$ and $\sigma^{\mathscr{L}} = 0.22$, calculated as the root mean square (RMS) between the actual ζ_2 values and the best-fit lines, and shown as shaded grey areas.

4.0.1.4 Ion chemistry and physical correlations

Fig. (4.0.6) shows the radial profiles from column density maps of HCO^+, N_2H^+, DCO^+, N_2D^+, and o-H_2D^+, including ζ_2 for the inner 0.1 pc of the simulated prestellar core, with each panel comparing the $\mathscr{H}$, $\mathscr{L}$, and $\mathscr{C}$ models at 153.3 kyr. To calculate the column densities, the gas cloud was integrated along a LOS aligned with the z-axis over a depth of 0.2 pc. To remove background particles from the integration, all gas particles that do not satisfy the condition $\log[n/(\mathrm{cm^{-3}})] \geq -3.78$, with n calculated as $\rho(2.3m_\mathrm{p})^{-1}$ and m_p the proton mass, were excluded. The radial profiles were then computed in circular annuli from the integrated quantities (column densities) and average along LOS (ζ_2 maps shown in Fig. (4.0.3). Panel (f) clearly shows how the high-density region affects the CR ionisation rate, exhibiting the effect of the CR attenuation in the central part, and causing the ionisation rate from model $\mathscr{H}$ to approach that of the $\mathscr{C}$ model. As a consequence, and analogously to that behaviour, the column densities of the deuterated species approach each other. For the $\mathscr{L}$ model, the differences are more pronounced,

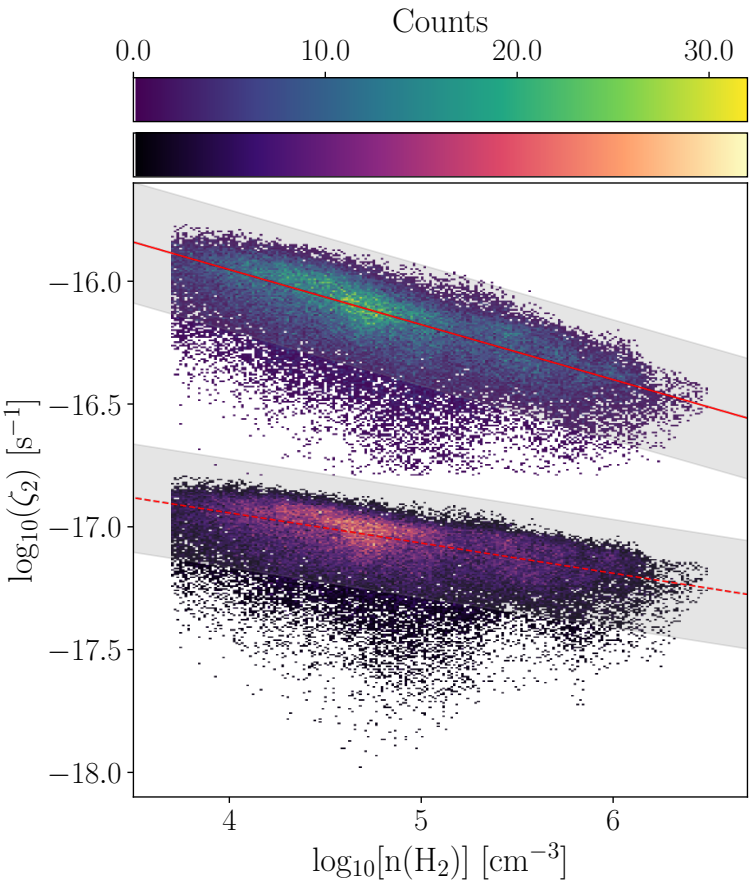

Figure 4.0.5: Correlation between ζ_2 and n(H_2) at 153.3 kyr. The viridis and magma color maps represent the $\mathscr{H}$ and $\mathscr{L}$ models, respectively. The solid and dashed red lines correspond to our best-fit relations, and the shaded areas show the intrinsic scatter discussed in Section 4.0.1.3.

specially for deuterated species such as DCO^+ and N_2D^+. In order to examine such differences, the fluxes (or efficiency) of the formation channels of each species were evaluated through the expression kn(A)n(B), where k denote the rate coefficient, and n(A), n(B) are the number densities of reactant A and B. It was found that reactions directly and strongly dependent on CR ionisation and deuterated species (H_2D^+, D_2H^+, and D_2^+) become much more relevant at high ionisation rate values by boosting N_2D^+, which in turn enhances the formation channel $CO + N_2D^+ \longrightarrow N_2 + DCO^+$. Therefore, the absence of a prominent peak in the DCO^+ radial profile is due to the low efficiency of its formation channels, particularly the aforementioned reaction, which is one of the main formation pathways for DCO^+.

As CRs are the only agent responsible for the ionisation of species in high density

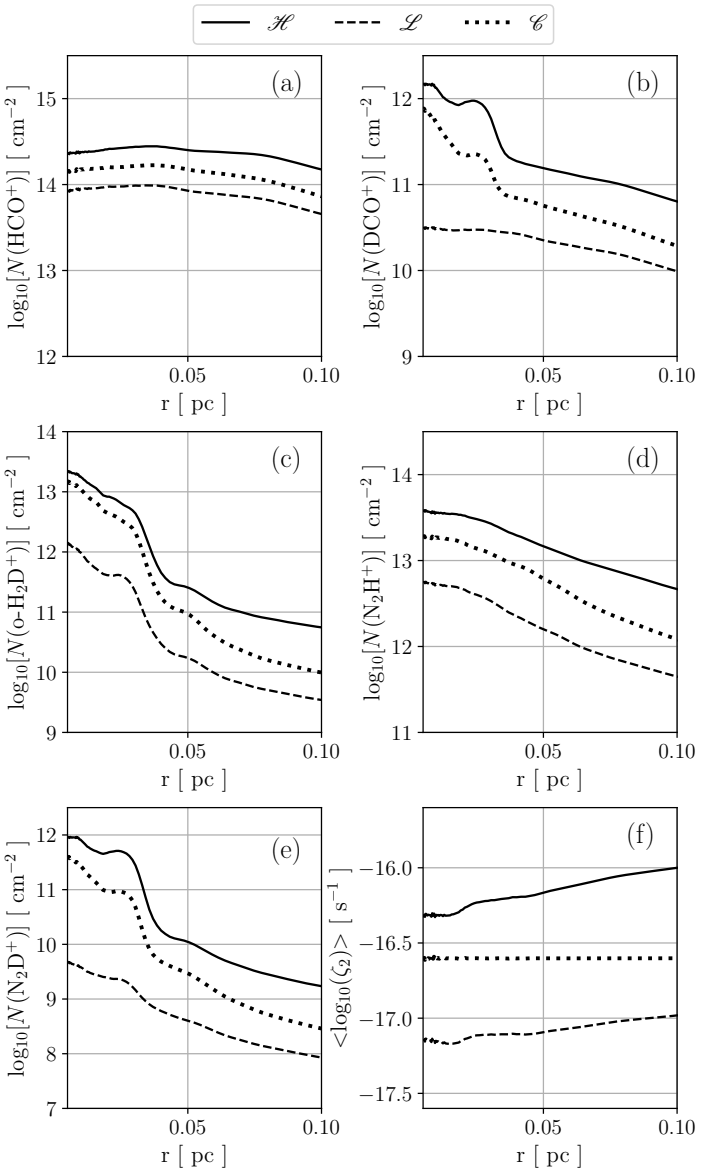

Figure 4.0.6: Radial profile of the column densities of the species HCO^+ (a), DCO^+ (b), o-H_2D^+ (c), N_2H^+ (d), N_2D^+ (e) ions and the ζ_2 distribution from Fig. (4.0.3) (f) at 153.3 kyr.

regions, the concentration of free electrons is expected to be tightly related to the degree of ionisation rate. Therefore, the correlation between the electron abundance, $X(\mathrm{e^-})$, and ζ_2 over time for $\mathscr{H}$ and $\mathscr{L}$ models is shown in Fig. (4.0.7). The abundance was calculated from the H_2 and e^- column densities along a LOS aligned with the z-axis, and defined as $X(\mathrm{mol}) = N(\mathrm{mol})/N(\mathrm{H_2})$. Both distributions exhibit a clear linear correlation that remains stable over time, indicating that when the amount of electron abundance is high (or low), the

degree of CR ionisation rate should be correspondingly high (or low). The distributions were fitted with a power law of the form

$$\log_{10}\zeta_2^{\mathscr{H}} = 0.41\log_{10}X(\mathrm{e}^-) - 13.06, \tag{4.0.3}$$

$$\log_{10}\zeta_2^{\mathscr{L}} = 0.32\log_{10}X(\mathrm{e}^-) - 14.53. \tag{4.0.4}$$

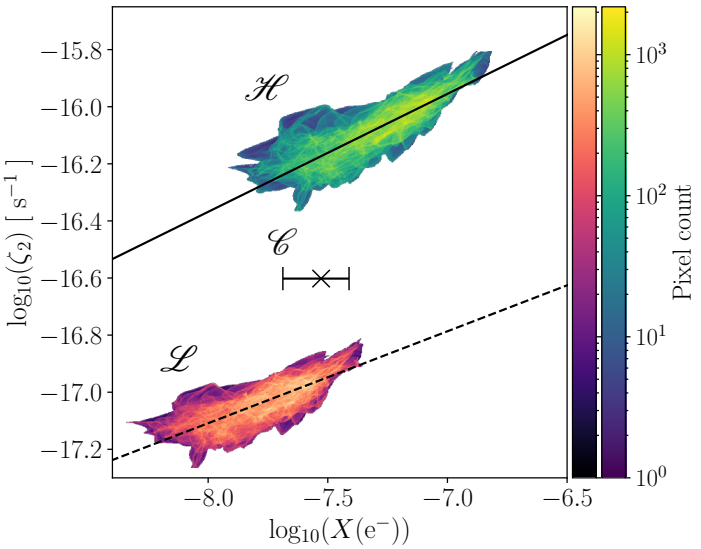

Figure 4.0.7: Correlation between $X(e^-)$ and ζ_2 obtained from the 2D maps for models $\mathscr{H}$ and $\mathscr{L}$, combining different time snapshots ($t = 30.7,\ 95.0,\ 153.3$ kyr). The solid and dashed lines correspond to power-law fits. The cross located at $\log_{10}(\zeta_2) = -16.6$ represents the median of the electro abundance ($X(\mathrm{e}^-)$) for the $\mathscr{C}$, and the error bars are the 1σ of the data.

Similarly, a linear correlation is also expected between the electron abundance (or column density) and the sum of the main positive ions (DCO^+, HCO^+, N_2H^+, N_2D^+, and H_3^+). Unfortunately, H_3^+ is not observable in the dense and cold regions of MCs, it was threfore replaced with the proxy proposed by Bovino et al. (2020):

$$N(\mathrm{H}_3^+)_{\mathrm{proxy}} = \frac{1}{3}\frac{\mathrm{N(o-H_2D^+)}}{\mathrm{R_D}}, \tag{4.0.5}$$

where R_D is the deuterium fractionation of HCO^+

$$R_\mathrm{D} = \frac{N(\mathrm{DCO^+})}{N(\mathrm{HCO^+})}. \tag{4.0.6}$$

Then, using Eqs. (4.0.5),(4.0.6), the following expression was tested to evaluate its reliability when applied to observational data:

$$N(e^-)_{\rm proxy} = N({\rm DCO^+}) + {\rm N(HCO^+)} + {\rm N(N_2D^+)} + N({\rm N_2H^+}) + {\rm N(H_3^+)_{proxy}}. \quad (4.0.7)$$

The distributions of H_3^+ and e^- compared against their proxies (Eqs. (4.0.5),(4.0.7)) for models $\mathscr{H}$ and $\mathscr{L}$ averaged over time are shown in Fig 4.0.8. The $N(H_3^+)$-$N(H_3^+)_{\rm proxy}$ panel exhibits a very tight linear correlation up to approximately $10^{13} - 10^{14}$ cm^{-2} for both models, beyond which a steeper linear deviation appears, corresponding to the central 10.000 au and likely caused by the neglected isotopologues in the H_3^+ estimation. A similar behaviour is also observed for the $N(e^-)$-$N(e^-)_{\rm proxy}$ panel. An RMS error analysis was used to quantify the discrepancy between the true e^- abundance and its proxy, computed as the ratio between $N(e^-)_{\rm proxy}$ and the actual $N(e^-)$, resulting in a 65% underestimation of the true e^- abundance. This difference arises from the limited number of ions considered in Eq. (4.0.7) and the approximations made. At first glance, the simulation of a typical prestellar core on sub-parsec scales was employed to validate the formula provided in Eq. (4.0.7). Nevertheless, it also holds on larger scales and exhibits wider applicability. The factors supporting the this statement are: (i) the omission of potentially relevant ions, such as H_3O^+; (ii) the exclusion of charged grains, which alter the negative charge balance and may be important for star-forming regions; (iii) the H_3^+ proxy formula does not include the column densities of other isotopologues (D_2H^+ and D_3^+), which become important as the central core density increases (Bovino et al., 2020); (iv) the use of averaged quantities (column densities) to estimate local physical variables. For the aforementioned reasons, the estimates of the ionisation fraction provided constitute a robust tool for determining a lower limit of the true value.

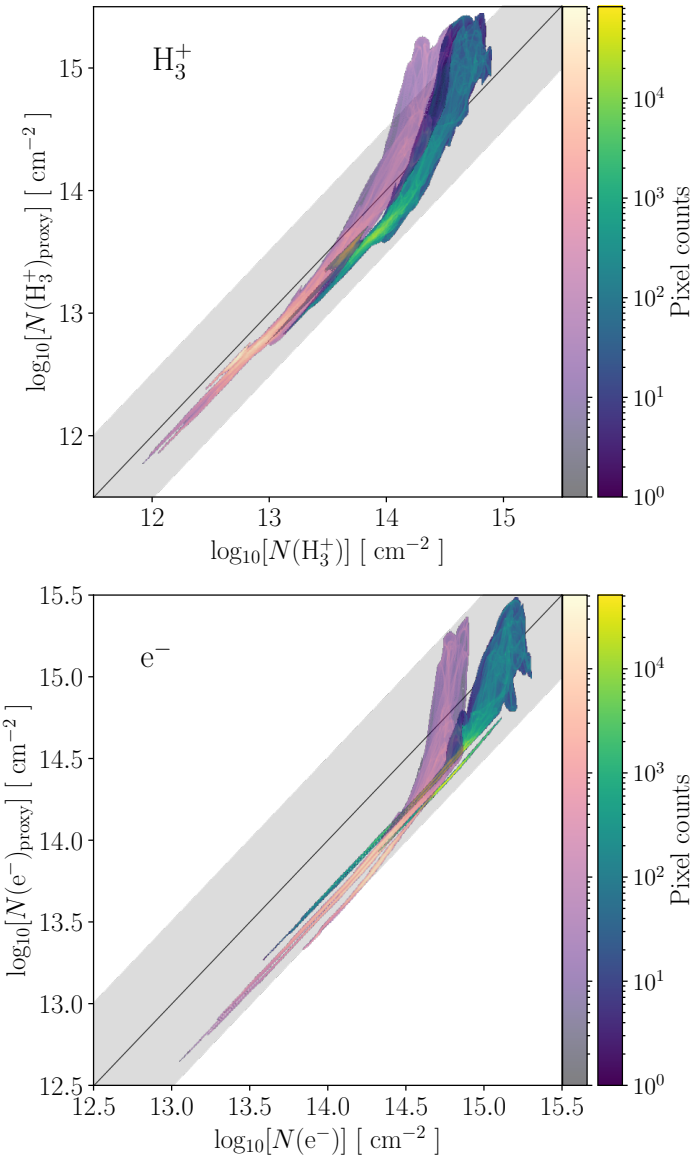

Figure 4.0.8: Pixel-by-pixel 2D histogram distributions for the $\mathscr{H}$ (viridis) and $\mathscr{L}$ (magma) model by combining different times (t=30.7, 95.0, 153.3 kyr). The upper panel correlates the H_3^+ column density from KROME and its proxy calculated by Eq. (4.0.5). The bottom panel shows the correlation between the e^- column density and its proxy calculated by Eq. (4.0.7). The solid black line in both panels represents a 1:1 straight line and serves as an indicator for the lineal correlation formed by the 2D histogram distributions. The grey shadow indicates a region spanning one order of magnitude (-0.5 and +0.5) around the 1:1 black line.

4.0.1.5 Observational application

To assess the applicability of Eq. (4.0.7), it was applied to a sample of 20 low-mass prestellar cores (R2025; Redaelli et al., 2025) located within $\lesssim 250$ pc and embedded in the following parental clouds: Taurus (Tau #, TMC1-C^e, L1544), Ophiuchus (Oph 1-6 and D), Corona Australis (CrA #), and isolated cores (L183, L429, and L694-2). The work by R2025 focused on measuring the cosmic-ray ionisation rate of the sample, while also examining features such as the level of deuteration and the degree of ionisation. The selected sources, listed in Table (4.0.2), were observed with the Atacama Pathfinder EXperiment (APEX) as single points using the coordinates provided in Table (4.0.2), and employing different spectral setups:

- Setup 1 covered the o-$H_2D^+(1_{1,0}$-$1_{1,1})$ using the LAsma receiver,
- Setup 2 covered DCO^+ (3-2) and $C^{18}O$ (2-1) lines using the nFLASH230 receiver,
- Setup 3 covered $HC^{18}O^+$ and $H^{13}CO^+$ (2-1) lines using the SEPIA 180 receiver,
- Setup 4 covered the HCO^+ and $H^{13}CO^+$ lines using the nFLASH230 receiver.

All setups used the APEX FFTS spectrometer at 64 kHz resolution, corresponding to a velocity resolution of $0.05 - 0.11$ km s^{-1}. Figure 4.0.9 shows the column density maps for each source, obtained from the Herschel Gould Belt Survey (HGBS) and published maps (Spezzano et al., 2017; Redaelli et al., 2018). The HGBS provides H_2 column density maps at an angular resolution of 18.2", while the resolution for the published maps is larger, $\approx$ 37", which is closer to the APEX resolution at ~ 2 mm.

Core	Coordinates		Distance (pc)	$N(H_2)$ [cm^{-2}]
	RA (J2000)	Dec (J2000)		
Tau 410	$04^h18^m40.32^s$	$+28°28^m29.0^s$	130	1.8
Tau 420	$04^h18^m40.32^s$	$+28°23^m16.0^s$	130	4.0
TMC1-C[e]	$04^h41^m32.31^s$	$+26°00^m40.0^s$	140	1.9
L1544	$05^h04^m17.21^s$	$+25°10^m42.8^s$	170	11.6
L183	$15^h54^m08.56^s$	$-02°52^m49.0^s$	110	5.9
L429	$18^h17^m05.53^s$	$-08°13^m29.9^s$	200	5.1
L694-2	$19^h41^m05.03^s$	$+10°57^m02.0^s$	250	4.3
Oph 1	$16^h31^m57.63^s$	$-24°57^m49.0^s$	140	3.8
Oph 2	$16^h31^m39.94^s$	$-24°49^m50.3^s$	140	5.2
Oph 3	$16^h27^m33.24^s$	$-24°26^m24.1^s$	140	7.8
Oph 4	$16^h27^m12.77^s$	$-24°29^m40.3^s$	140	5.6
Oph 5	$16^h27^m15.28^s$	$-24°30^m30.1^s$	140	5.4
Oph 6	$16^h27^m19.99^s$	$-24°27^m17.6^s$	140	4.7
Oph D	$16^h28^m28.56^s$	$-24°19^m25.0^s$	140	1.7
CrA 038	$19^h01^m46.10^s$	$-36°55^m35.7^s$	150	6.2
CrA 040	$19^h01^m47.28^s$	$-36°56^m39.8^s$	150	4.6
CrA 044	$19^h01^m54.45^s$	$-36°56^m39.8^s$	150	10.5
CrA 047	$19^h01^m55.86^s$	$-36°57^m46.9^s$	150	9.9
CrA 050[g]	$19^h01^m58.94^s$	$-36°57^m09.9^s$	150	3.5
CrA 151	$19^h10^m20.17^s$	$-37°08^m27.0^s$	150	4.1

Table 4.0.2: Names, coordinates, distances, and total column densities (in terms of 10^{22} cm^{-2}) of the sources.

The use of APEX serves to retrieve the cosmic-ray ionisation rate value through the analytical formula introduced in Bovino et al. (2020):

$$\zeta_2 = k_{CO}^{oH_3^+} \times X(CO) \times \frac{N(o-H_2D^+)}{R_D} \frac{1}{L}, \tag{4.0.8}$$

where $k_{CO}^{oH_3^+}$ is the destruction rate of o-H_3^+ by CO and assumed to be the main destruction channel, $X(CO)$ is the CO abundance relative to H_2 determined as $X(CO) = N(CO)/N(H_2)$, R_D is the deuteration in Eq. (4.0.6), and L is the path length used to determine column densities. The advantage of this formula lies in its observational applicability and its model independence, enabling a reliable estimate of ζ_2 using observational data from instruments. This motivated the use of APEX for its determination, while also leveraging previously available data from the same instrument (Bovino et al., 2021).

The determination of molecular column densities followed the constant excitation temperature approach to fit the observed spectra using PYSPECKIT. The code fits the spectra using the following free parameters: the line centroid ($V_{\rm lsr}$), the line velocity dispersion ($\sigma_{\rm V}$), the molecular column density ($N_{\rm col}$), and the excitation temperature ($T_{\rm ex}$); when two transitions of the same species are available, the code assumes a single $T_{\rm ex}$ for all transitions, allowing $T_{\rm ex}$ and $N_{\rm col}$ to be fitted simultaneously.

Leveraging the molecular and total column density maps, R2025 measured the ionisation degree of the gas by determining the electron fraction (or abundance) $x(\mathrm{e}^-)$. Under the assumption that the charge of dust grains is negligible and free electrons are ceded by neutral species, Eq. (4.0.7) was applied using abundances instead of column densities. It is worth noting the lack of data for N-bearing species; however, the impact of these missing species is expected to be small since the main contributors come from the H_3^+ proxy and HCO^+. In Fig. (4.0.10), the resulting estimates are shown, with derived values ranging from $10^{-9} - 10^{-8}$. The majority of cores exhibit an ionisation fraction between $2 - 4 \times 10^{-9}$, which are in good agreement with results from the literature of similar sources (Caselli et al., 2002; Maret and Bergin, 2007).

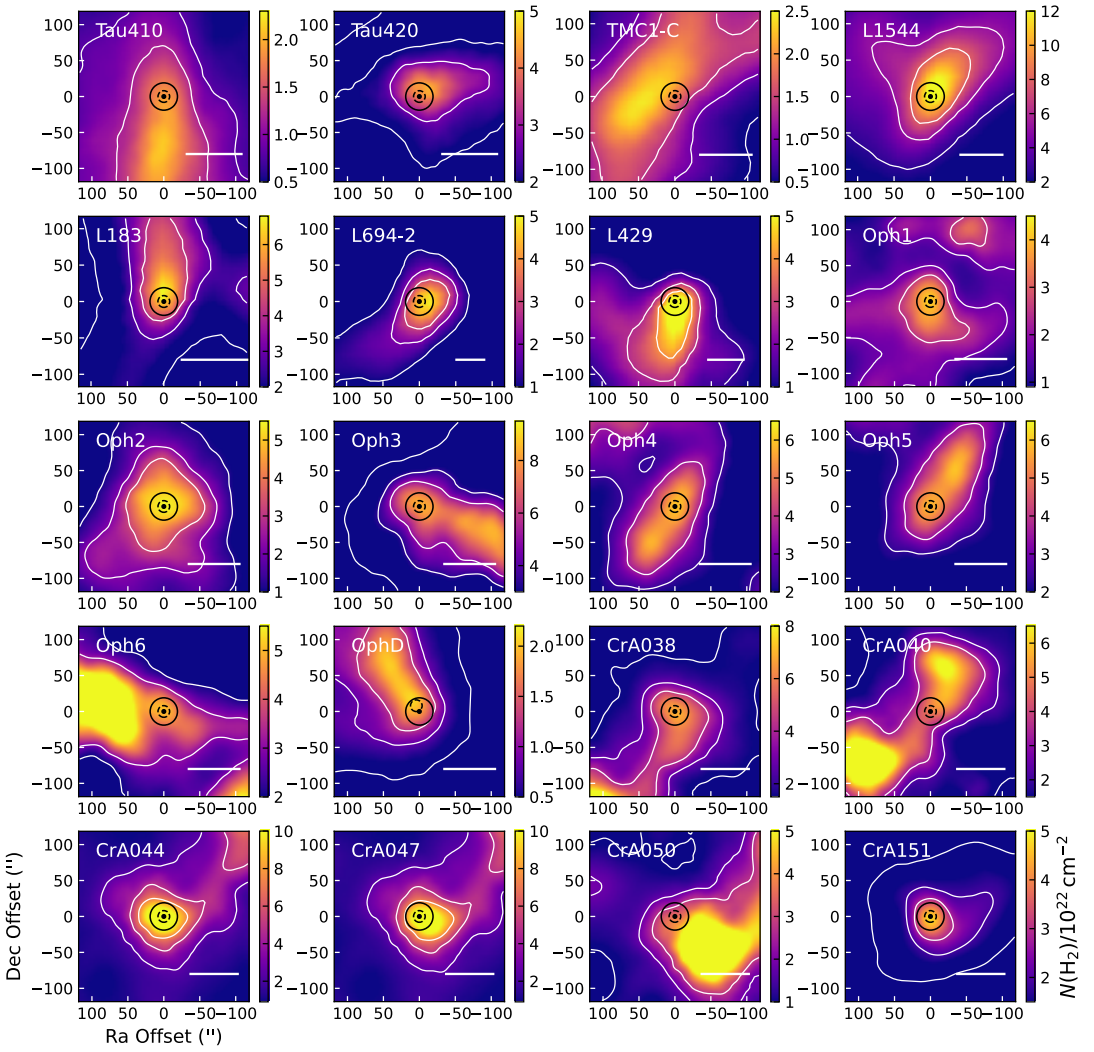

Figure 4.0.9: H_2 column density maps of each source in square regions of 4'×4' around the cores (Redaelli et al., 2025). The correspondent name of each source is located at the top-left corner on each subplot. The black solid circles indicate the APEX pointing and the $N(H_2)$ map beam size, while the dashed circles show the beam sizes and APEX pointing for o-H_2D^+ line. The white bar at the bottom-right corner represents a length of 0.05 pc. The white contours indicate the 20, 40, and 60% levels of the peak value within the central Herschel beam (37").

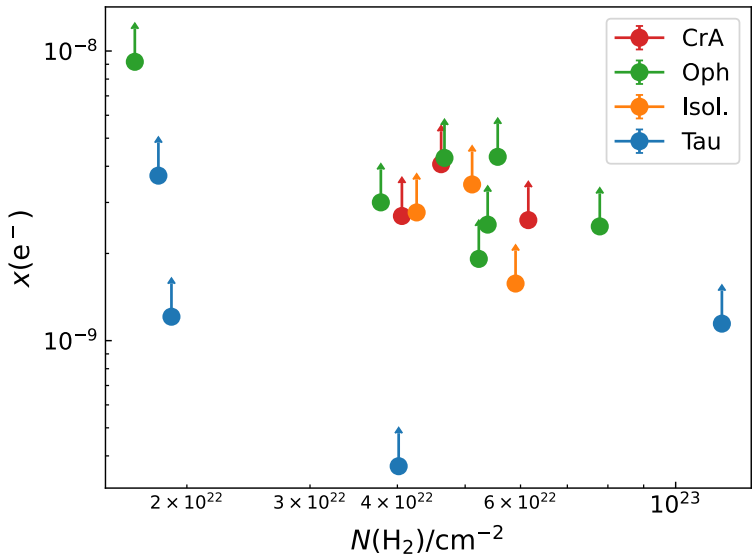

Figure 4.0.10: Estimated ionisation fraction with Eq. (4.0.7) as a function of central total column densities of cores. The $N(H_2)$ data is taken from HGBS and also reported in Table (4.0.2). The absence of these targets is due to the non-detection of o-H_2D^+ emission. The red, green, blue colours represent the cores in the Corona Australis, Ophiuchus, Taurus, respectively, while orange represents isolated cores.

Moreover, since the ionisation degree is directly proportional to the timescale for ambipolar diffusion $t_{\rm AD}$, it is possible to assess the dynamical stability of the cores by estimating both $t_{\rm AD}$ and $t_{\rm ff}$. The former is estimated as (Spitzer, 1978; Shu et al., 1987):

$$t_{\rm AD} = 2.5 \times 10^{13} \times x(e^-) \text{ yr}, \tag{4.0.9}$$

while for the latter is

$$t_{\rm ff} = \sqrt{\frac{3\pi}{32 G \mu m_{\rm H} n(H_2)}}, \tag{4.0.10}$$

where μ is the mean molecular of the gas set at 2.33, while $n(H_2) = N(H_2)/0.1$ pc ($N(H_2)$ from Table (4.0.2)), $m_{\rm H}$ the proton mass and G the gravitational constant. The comparison between the two timescales is showed in Fig. (4.0.11). Due to the lack of N-bearing species and other likely relevant ionised species and isotopologues such as H_3O^+ and D_2H^+, the approach used to calculate $x(e^-)$,

and consequently $t_{\rm AD}$, represent lower limits to their true values. Similarly, the approach used to compute $t_{\rm ff}$ underestimates the true central densities of the cores because it involves column density values that assume a constant volume density along LOS and are averaged over the Herschel beam size. Despite these limitations, the derived $t_{\rm AD}$ values are generally consistent with, or larger than, the corresponding $t_{\rm ff}$. In particular, the values obtained for the Ophiuchus cores are in good agreement with Bovino et al. (2021), who found that these sources are consistent with fast-collapse models, occurring on timescales shorter than those of ambipolar diffusion.

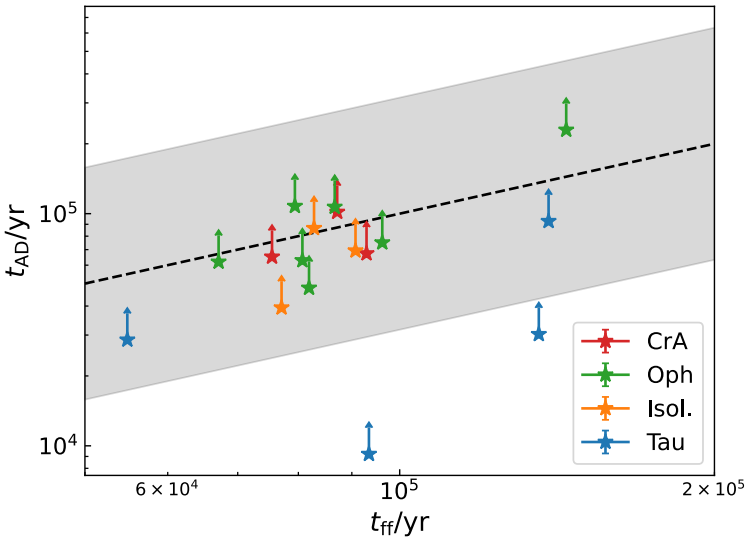

Figure 4.0.11: Determined ambipolar diffusion timescale ($t_{\rm AD}$) as function of the free-fall time ($t_{\rm ff}$). The colours are equivalent as Fig. (4.0.10). The dashed line indicates the 1:1 relation, and the shaded area represents the 0.5 dex scatter corresponding to the deviation shown in Fig. 4.0.8.

4.0.2 STARFORGE-KROME simulations

4.0.2.1 Density profile of relevant species

The new chemical network (hereafter referred to as custom network) was tested by comparing the abundance profile of several relevant species against those obtained with the chemical network developed by Semenov et al. (2010) (hereafter referred as solid network). As previously stated, that network includes $\sim$ 5000 reactions and is strongly oriented towards solid-phase chemistry consisting of gas-grain interactions and surface reactions. This comparison serves to verify

the evolution of species, particularly adsorbed species, under constant-density conditions. Moreover, it is motivated by the fact that the solid network provides a more comprehensive description and characterisation of the ISM due to its large number of species and reactions. In contrast, the custom network developed in this work contains about 6.7 times less reactions. Therefore, comparing its results allows us to assess its reliability in reproducing and characterising well-established results from the literature.

The KROME library was used to perform the time-evolution tests of the networks, corresponding to the one zone (1D) test following Section 4.1 from Grassi et al. (2017), which is based on Semenov et al. (2010). These tests aim to reproduce MC conditions, where the density and temperature remain constant, while the abundances of the chemical species evolve according to the non-equilibrium ODE system generated from the networks. The initial conditions start with a constant gas temperature of 10 K (adsorption case) and another case with 100 K (desorption case), a hydrogen number density of $n(\mathrm{H}) = 2 \times 10^4$ cm^{-3}, a CR ionisation rate set to 1.3×10^{-17} s^{-1}, dust-to-gas ratio of 0.01, dust density of $\rho_\mathrm{d} = 3$ g cm^{-3}, and an average grain of being 0.1 μm. The initial abundances of the elemental species are listed in Table (4.0.3), where the electron abundance is determined by summing the number densities of all ions, neglecting those atomic species not included in the custom network. The photobins are set similarly to those of STARFORGE, with bin limits in eV are defined as [0.75, 5.60, 8.0, 11.2, 13.6, 15.2, 24.59, 54.42, 100.6, 200, 10^3, 10^4]. For the solid network, the rate coefficients for photoreactions are determined using Eq. (1.3.4) instead of photobins, with an attenuation set to $A_v = 10$ mag. In contrast, the attenuation due to dust extinction in the custom network is determined using the model presented in Calzetti et al. (2000), given by:

$$f_\mathrm{obs} = f_\mathrm{int}(\lambda) 10^{-0.4 A_\lambda} \tag{4.0.11}$$

where f_obs, f_int are the observed and intrinsic fluxes, A_λ is the extinction at the wavelength λ, which is related to the reddening curve $k(\lambda)$ as

$$A_\lambda = \frac{k(\lambda) A_V}{R_V}, \tag{4.0.12}$$

Species	$n(X)/n_{\rm H}$	Species	$n(X)/n_{\rm H}$
He	9.00×10^{-2}	H_2	5.00×10^{-1}
C^+	1.20×10^{-4}	N	7.60×10^{-5}
O	2.56×10^{-4}	S^+	8.00×10^{-8}
Si^+	8.00×10^{-9}	Na^+	2.00×10^{-9}
Mg^+	7.00×10^{-9}	Fe^+	3.00×10^{-9}
P^+	2.00×10^{-10}	Cl^+	1.00×10^{-9}

Table 4.0.3: Initial abundances taken from (Semenov et al., 2010) for one zone tests between the custom network and its network.

with R_V as the effective total obscuration (set to 3.1), A_V the extinction at V, and $k(\lambda)$ being:

$$k(\lambda) = \begin{cases} 2.659(-2.156 + \frac{1.509}{\lambda} - \frac{0.198}{\lambda^2} + \frac{0.011}{\lambda^3}) + R_V, & 0.12\ \mu\text{m} \leq \lambda \leq 0.63\ \mu\text{m}, \\ 2.659(-1.857 + \frac{1.040}{\lambda}) + R_V, & 0.63\ \mu\text{m} \leq \lambda \leq 2.20\ \mu\text{m}. \end{cases} \tag{4.0.13}$$

The comparison is carried out for sets of representative species that characterise the complete network. For the hydrogen, carbon, and nitrogen-bearing groups, the sets are defined as follows: (i) H_2, H_3^+, H_2O, HCO^+, and H_2O_d (icy water, where the subscript d denotes dust adsorption); (ii) C, C^+, and CO; (iii) N_2, NH_3, N_2H^+, NH_4^+. The evolution is followed over a time span of 1 Myr. In the first place, Fig. (4.0.12) shows the results of the comparison at a gas temperature of 10 K, that is, when the solid-phase chemistry is strong. The hydrogen group exhibits the total H_2, H_3^+ (determined as x(A$_2$)= x(o-A$_2$) + x(p-A$_2$) with A being H_2 or H_3^+) and $H_2O_{\rm dust}$ as the species with remarkable profile, while H_2O and HCO^+ struggle to reproduce the reference results at $t = 10$ kyr. Overall, the carbon group exhibits a satisfactory agreement up to 1 Myr, with only C and C^+ exhibiting noticeable discrepancies at ~ 0.1 Myr and 10 kyr, respectively. The nitrogen group reveals that N_2, N_2H^+, and NH_4^+ are consistent with the solid network, although N_2H^+ shows a different normalisation and NH_4^+ differs after $t = 10$ kyr, while NH_3 shows almost a different profile.

In the second case, Fig. (4.0.13) shows the results when most of the species adsorbed onto dust grains are desorbed due to the warm gas temperature of 100 K. Overall, across the three groups the lines profiles exhibit good (H_2O, H_2O_d, NH_3, N_2H^+) to excellent (H_2, C, C^+, CO, N_2, NH_4^+) agreement between the two

networks, with only a few species (H_3^+ and HCO^+) showing significant deviations. Icy water on the custom network is much more sensitive to desorption effects at this temperature than on the solid network, leading to its diminution at late times. Because H_3^+ reacts with a wide variety of atomic and molecular species, the custom network omits many of the reactions listed in Semenov et al. (2010), which are in principle included in the solid network. This limitation reduces the destruction channels of H_3^+, leading to a general overabundance in its predicted abundance.

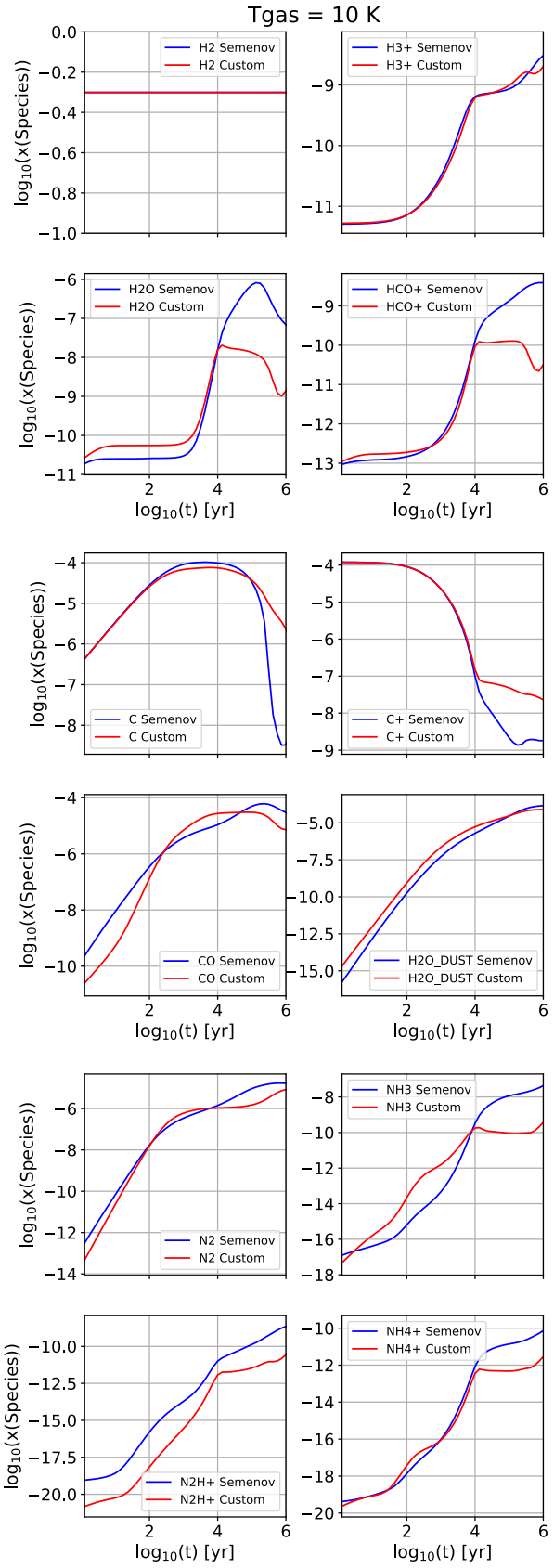

Figure 4.0.12: Temporal evolution of the abundances of certain species. The leftmost, middle, and right most panels represent the hydrogen, carbon, and nitrogen groups that account for the complete network. The red and blue curves are the custom and solid networks, respectively.

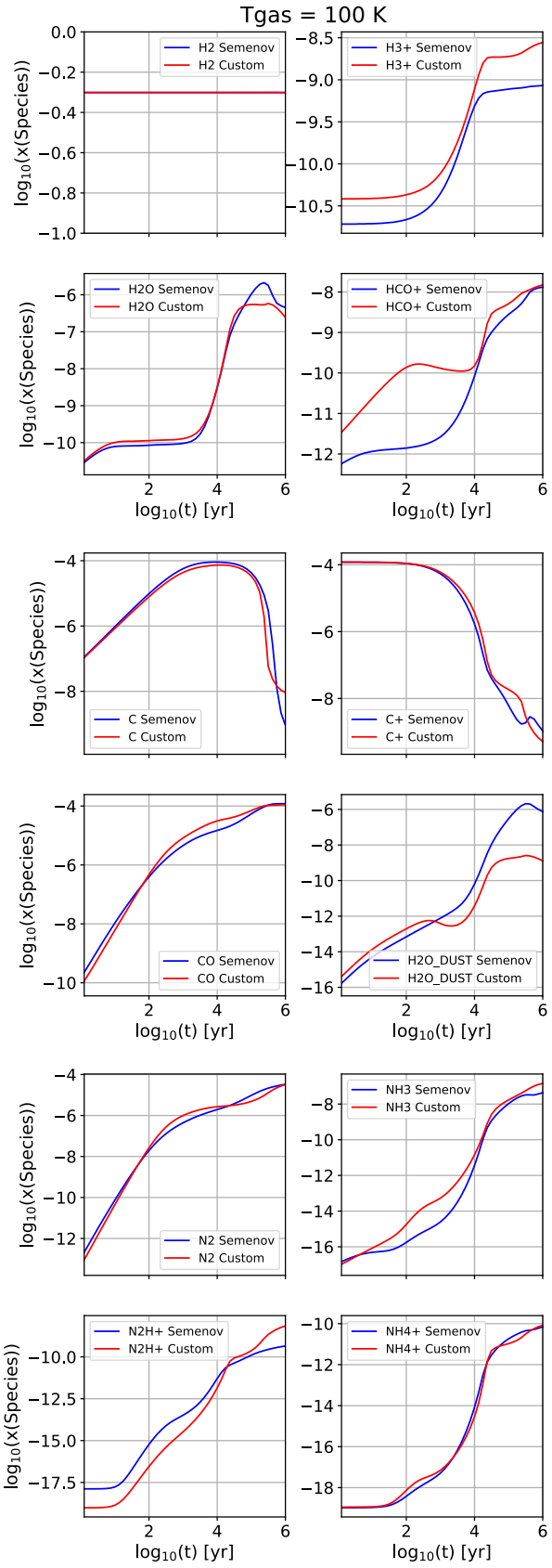

Figure 4.0.13: Temporal evolution of the abundances of certain species at 100 K, analogous to Fig. (4.0.13).

4.0.2.2 Thermal profile

The following test examines the thermal evolution produced by the custom network, particularly for its further use in the STARFORGE-KROME software. The one zone cloud collapse from KROME, based on Omukai et al. (2005), is employed (Section 4.2 in Grassi et al., 2014) for this purpose.

The test replicates the conditions used in Omukai et al. (2005), which in principle aimed to study the thermal (and chemical) evolution of star-forming regions at different metallicities while including detailed thermochemical microphysics. On one hand, the setup considers solar metallicity ($Z = 0$), gas temperature $T = 300$ K, total number density $n = 0.1$ cm^{-3}, and an initial H_2 abundance $y(H_2) = 10^{-6}$, as listed in Table (4.0.4). Carbon is fully ionised, while Helium and Oxygen are fully neutral. The following cooling mechanisms are included: atomic and molecular line radiation, continuous gas radiation, and cooling associated with chemical reactions. The heating mechanisms includes: compressional heating, H_2 formation heating, and heating produced by chemical reactions. On the other hand, additional aspects must be considered due to the custom network. Specifically, other processes not considerated in Omukai et al. (2005) are now included, such as: the CR ionisation rate is set to 2.5×10^{-17} s^{-1}, the dust-to-solar ratio is 0.01, the grain bulk density is set to $\rho_0 = 3$ g cm^{-3}, and the average grain size of 0.1 μm. The photobin limits (eV) are defined as [0.75, 5.60, 8.0, 11.2, 13.6, 15.2, 24.59, 54.42, 100.6, 200, 10^3, 10^4]. The implemented cooling mechanisms include dust thermal emission, CO molecular line, atomic cooling by collisional ionisation and excitation, recombination and dielectric recombination of atomic species (H and He both neutral and ionised), bremsstrahlung emission, metal line cooling. The heating processes considered are: photoelectric effect on dust, CR heating, and photoheating , all summarised in Table (4.0.5). Opacity and dust temperature are determined using the tables approach from Grassi et al. (2017). To ensure numerical stability, a temperature floor of $T = 10$ K is added.

Species	$n(X)$
H^+	$n(H) \times 10^{-4}$
o-H_2	$0.75 \times n(H) \times 10^{-6}$
p-H_2	$0.25 \times n(H) \times 10^{-6}$
He	$0.0775 \times n(H)$

Table 4.0.4: Initial number densities of the species for one zone collapse tests for the custom network.

Cooling		
Process	Species involved	Formula
Atomic	H, H^+, He, He^+	(2.2.2)-(2.2.12)
Molecular	o/p-H_2	(2.2.13)-(2.2.19)
Metals	CO, CI, CII, OI, OII, SiI, SiII	(2.2.24)
Bremsstrahlung	H^+, He^+, C^+, O^+, N^+, Si^+, He^{++}, Si^{++}	(2.2.29)
Compton	e^-	(2.2.25)
Chemical	H, H^+, He, He^+, He^{++}, H_2, e^-	(2.2.22),(2.2.23)
Dust		(2.2.28)
Heating		
Process	Species involved	Formula
Chemical	H, H^-, H_2, H_2^+	(2.2.30)-(2.2.36)
Cosmic-ray	ionised by CRs	(2.2.38)
Photoelectric	H, e^-	(2.2.40)
Radiation	ionised by photons	(2.2.37)

Table 4.0.5: Cooling and heating mechanisms included in the test. The left, middle and right column represent the process of the mechanism, the species involved in each mechanism when correspond, and the formula referenced for its calculation.

The resulting thermal profile is shown in Fig. (4.0.14) and compared with two thermal profiles derived by Omukai et al. (2005). The profile exhibits an initial rise in gas temperature, followed by a gradual decline around $\log_{10}(\mathrm{ntot}) \approx 2$. This behaviour originates from the inclusion of new photoreactions that introduce additional channels for the production of free electrons, thereby enhancing the photoelectric heating, which simultaneously competes with metal cooling. The steeper decline between $1.7 \lesssim \log_{10}(\mathrm{ntot}) < 3$ marks the point where metal cooling becomes dominant over the heating generated by the photoelectric effect on dust. A small bump at $\log_{10}(\mathrm{ntot}) \approx 4$ appears when metal line cooling ceases to be efficient, and cosmic-ray heating becomes dominant, pushing the gas temperature

slightly above the imposed floor of 10 K. Beyond this point, the dust radiatively cooling recombination takes over and counteracts the compressional heating.

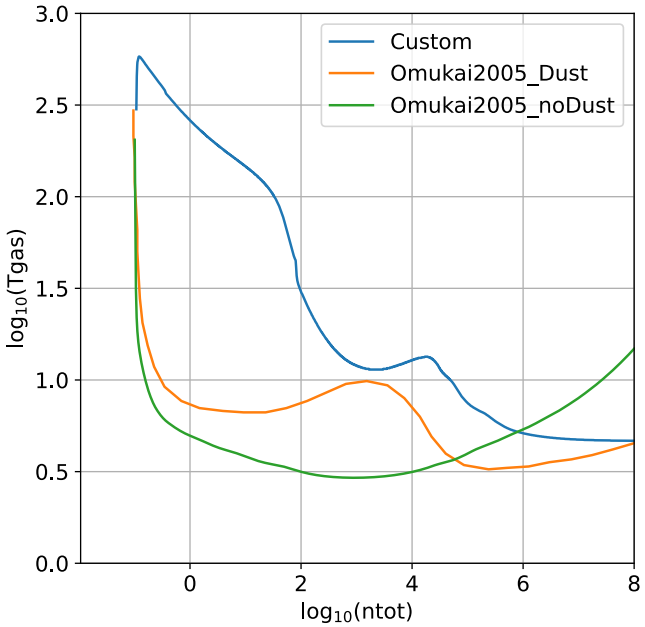

Figure 4.0.14: Thermal profiles of the custom network (blue line) and the two tests carried out in Omukai et al. (2005), with (orange line) and without dust (green line).

4.0.2.3 First simulation results

The numerical radiative magnetohydrodynamic simulation of a GMC was performed using STARFORGE. To incorporate detailed microphysics into the simulation, the software was coupled with the thermo-chemistry library KROME. The coupled software, STARFORGE-KROME, allows computing the dynamical evolution of the cloud alongside detailed microphysics on-the-fly, specifically solving ODEs constructed from the chemical network, as well as the cooling, heating, and thermal evolution of the cloud. The simulation follows the evolution of a GMC from its formation to its dispersion, including the previously defined radiation bands and all forms of stellar feedback, that is, jets, stellar winds, SNe, and radiation. The chemical characterisation and initial conditions, such as abundance of species, CR ionisation rate, among others, are analogous to those presented in Section 4.0.2.2, while also including the corresponding cooling and heating processes.

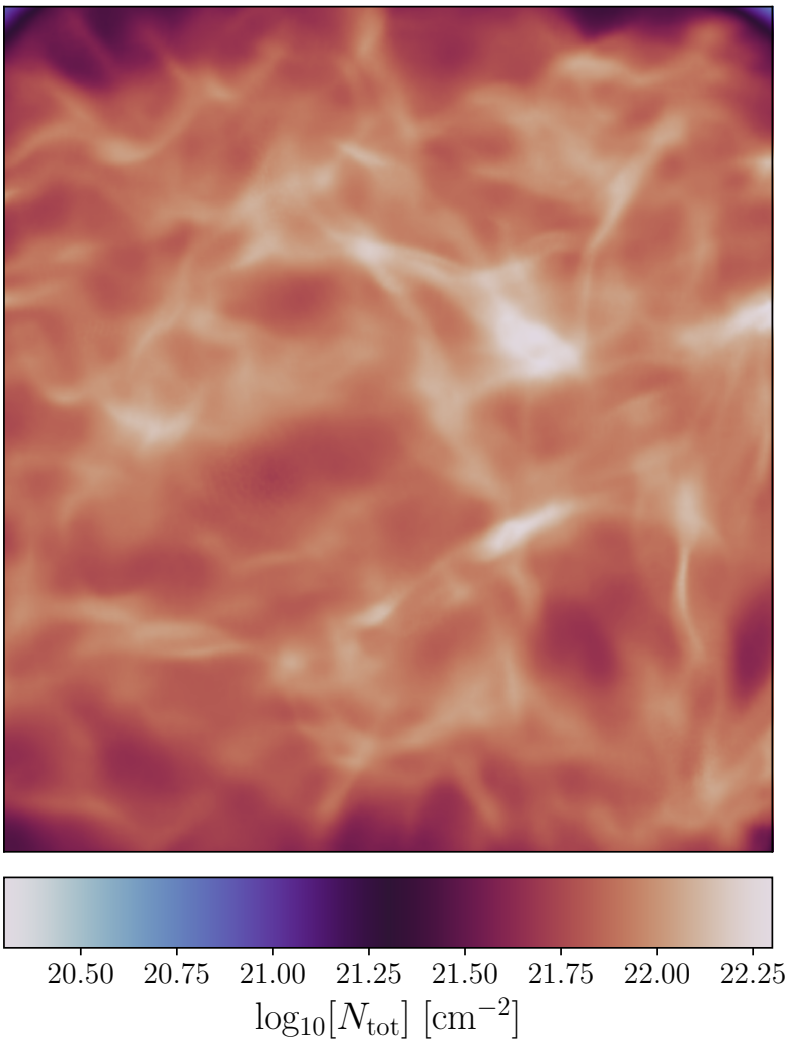

Figure 4.0.15: Total column density map of the central region integrated over the entire cloud at z-axis (8 pc) at 0.225 Myr. The view spans 4×4 pc^2.

The total column density of the cloud ($N_{\rm tot}$) is shown in Fig. 4.0.15. It spans 4×4 pc^2 and represents the central region of the cloud, integrated over 8 pc along the z-axis, which encompasses the entire cloud at 0.225 Myr. The displayed region contains dense gas ($> 10^{21}$ cm^{-2}). The filamentary structure lies in the range $\sim 10^{21.5-22}$ cm^{-2}, with a few spots located on the right side reaching $\sim 10^{22.25}$ cm^{-2}, which are likely the next sites of star formation. Moreover, Fig. 4.0.16 shows the ρ-weighted thermal map of the same region, where a prominent filament emerges crossing the cloud from south to north and several other filaments branches horizontally from it. The revealed structure identifies filaments as cold as ~ 14 K,

matching those appreciable on Fig. 4.0.15, while several clumps are seen in between at $\sim$ 20K.

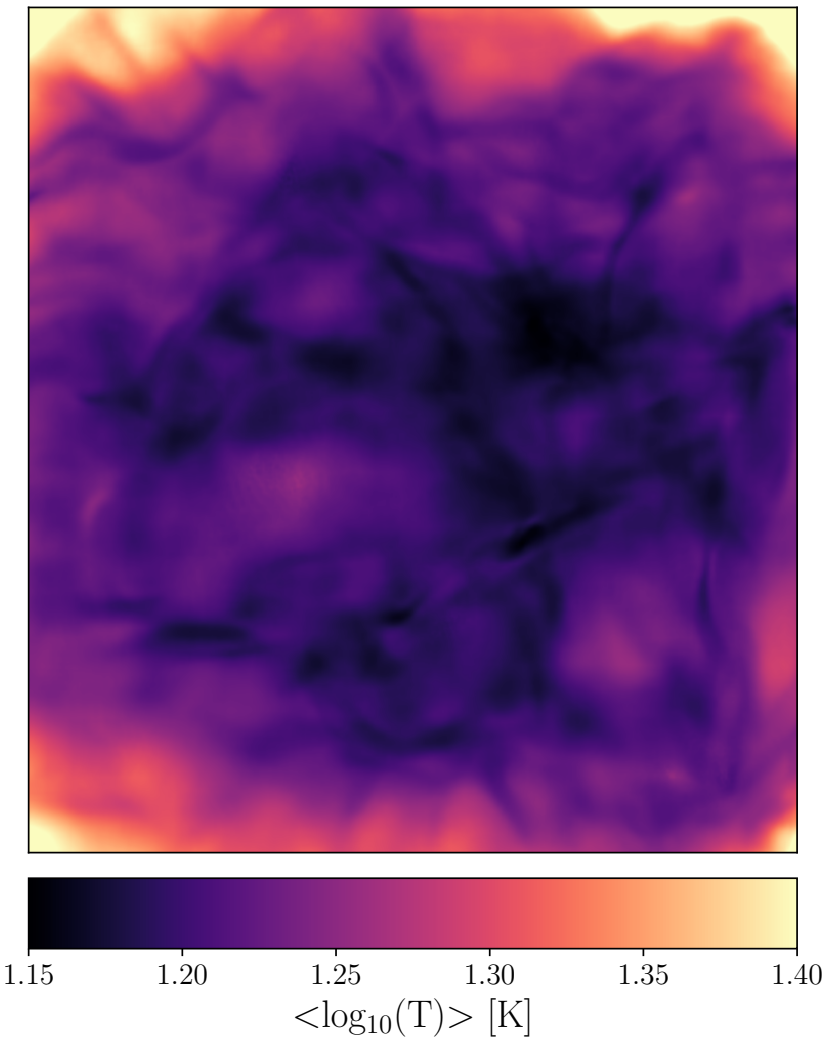

Figure 4.0.16: Density-weighted thermal map of the central region of the cloud, spanning 4×4 pc^2 at 0.225 Myr.

Similarly, Figs. (4.0.17) and (4.0.20) exhibit column density maps of key relevant species in the network: H_2, H_3^+, C, H_2O, CO, C^+, HCO^+, NH_3, NH_4^+, N_2O, N_2H^+, H_2O_{dust}. The structure displayed in the H_2 map accurately follows the total column density map, while H_3^+ map denotes the ionised structure present in the cloud localised at the centre. Moreover, C^+ demonstrate that is more numerous at the boundary of the cloud where low-density regions lie, indirectly implying where high density regions and ionised (in less degree) should locate, matching the prior

two maps. Analogously, N_2H^+ points directly to the regions of intense ionisation, where only three small regions are capable to form NH_3 and NH_4^+ numerously. Moreover, the concentration of Icy water spikes only in such small regions, strongly suggesting that these are indeed upcoming star-forming sites. On the other hand, the lack of $N(\mathrm{CO})$ content compared to $N(\mathrm{C})$ indicates adsorption effects.

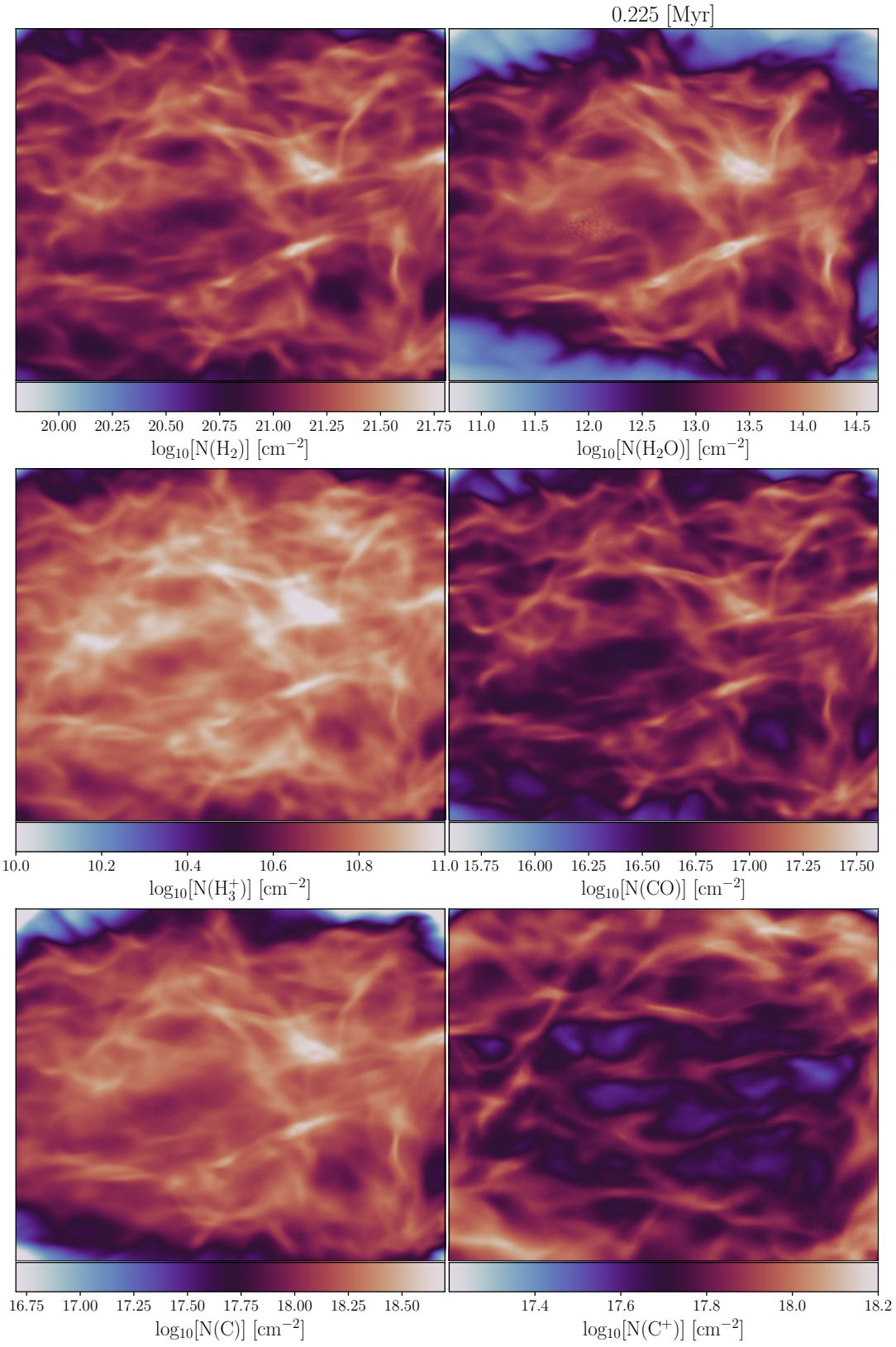

Figure 4.0.17: Column density maps of several species at 0.225 Myr. From top to bottom, the first column shows H_2, H_3^+, C; while the second column shows H_2O, CO, C^+.

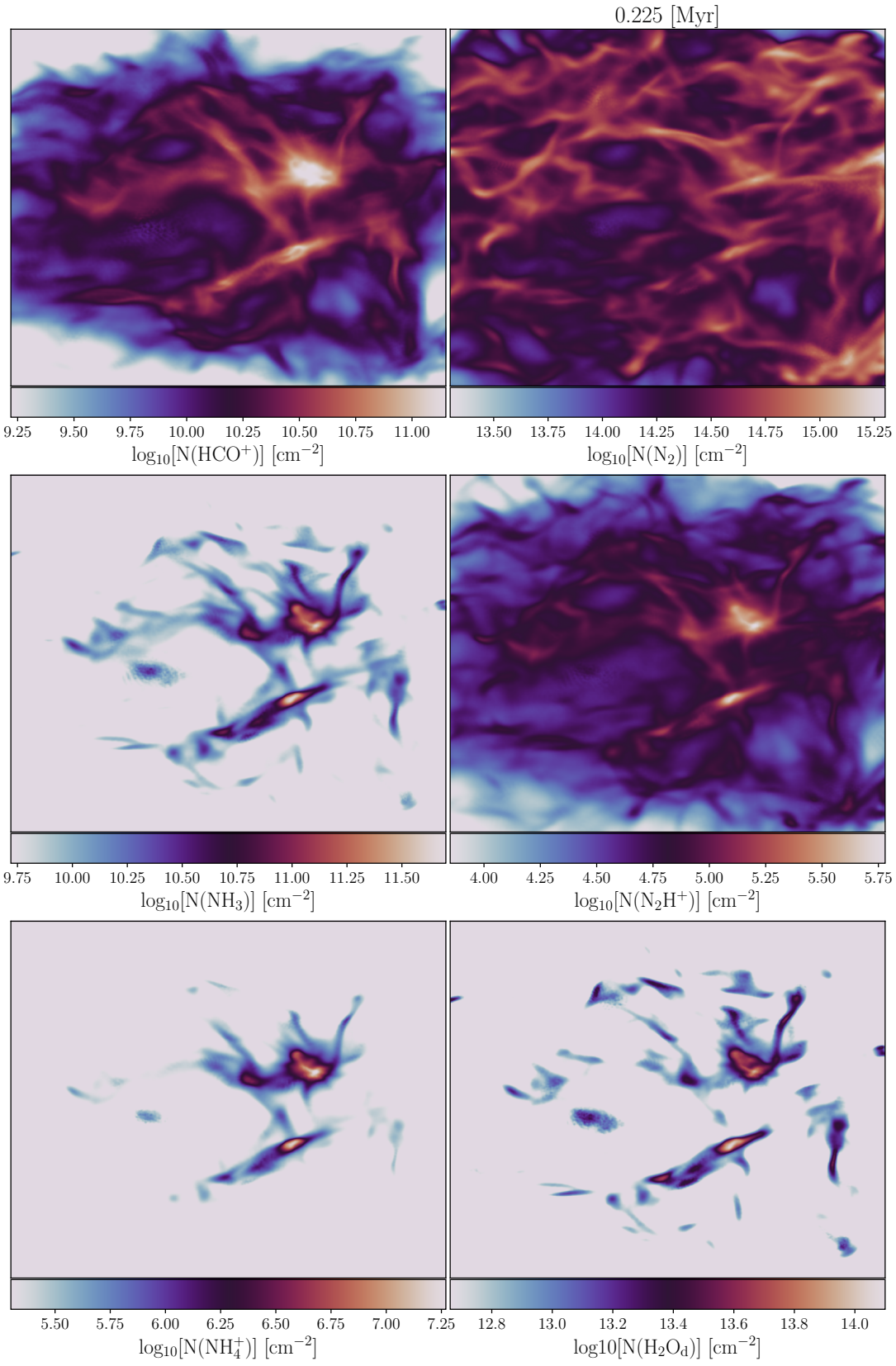

Figure 4.0.18: Continuation of Fig. 4.0.17. It displays column density maps of several species at 0.225 Myr. From top to bottom, the first column shows HCO^+, NH_3, NH_4^+; while the second column shows N_2O, N_2H^+, H_2O_{dust}.

Figures (4.0.19) and (4.0.20) show the abundance profile of key species H_2, H_3^+, HCO^+, H_2O, C, C^+, CO, H_2O_{dust}, N_2, NH_3, N_2H^+, and NH_4^+, at 0.225 Myr and centred on the region of highest density within a $4 \times 4 \times 4$ pc^{-3} box. An additional simulation was performed with STARFORGE-KROME using another network. This network is gas-phase oriented and does not include the ortho-para branch, photobins, or surface chemistry, yet it provides a suitable comparison for gas-phase species. The resulting distributions show overall reasonable agreement. For completeness, the 2d distributions of the remaining species without a direct comparison are also shown, with all of them exhibiting absence of non-standard and unexpected features.

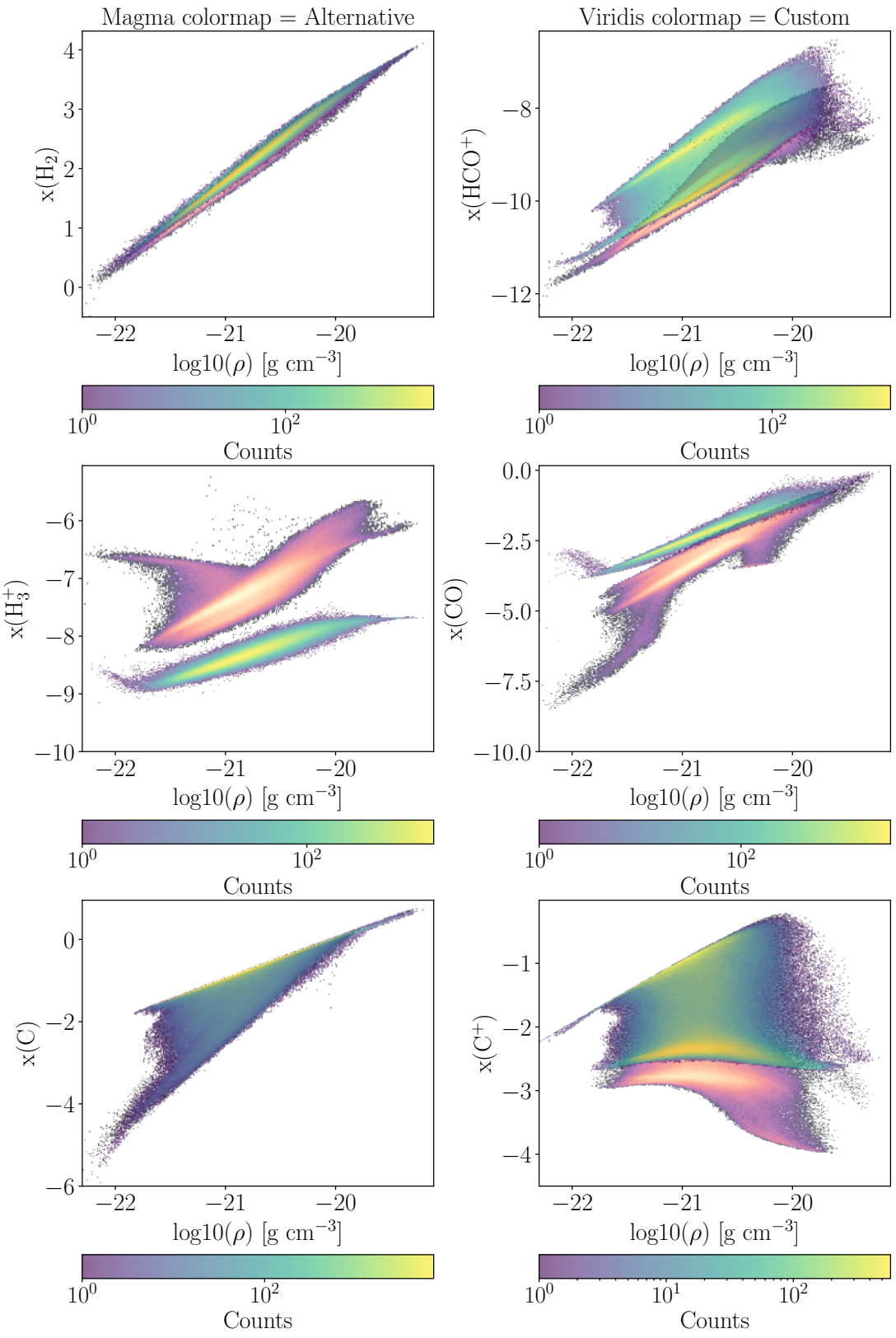

Figure 4.0.19: 2D distributions of several species representative of the entire network at 0.225 Myr. The viridis and magma colour maps correspond to species from the custom and alternative networks, respectively. The species shown are H_2, H_2O, H_3^+, CO, C, C^+.

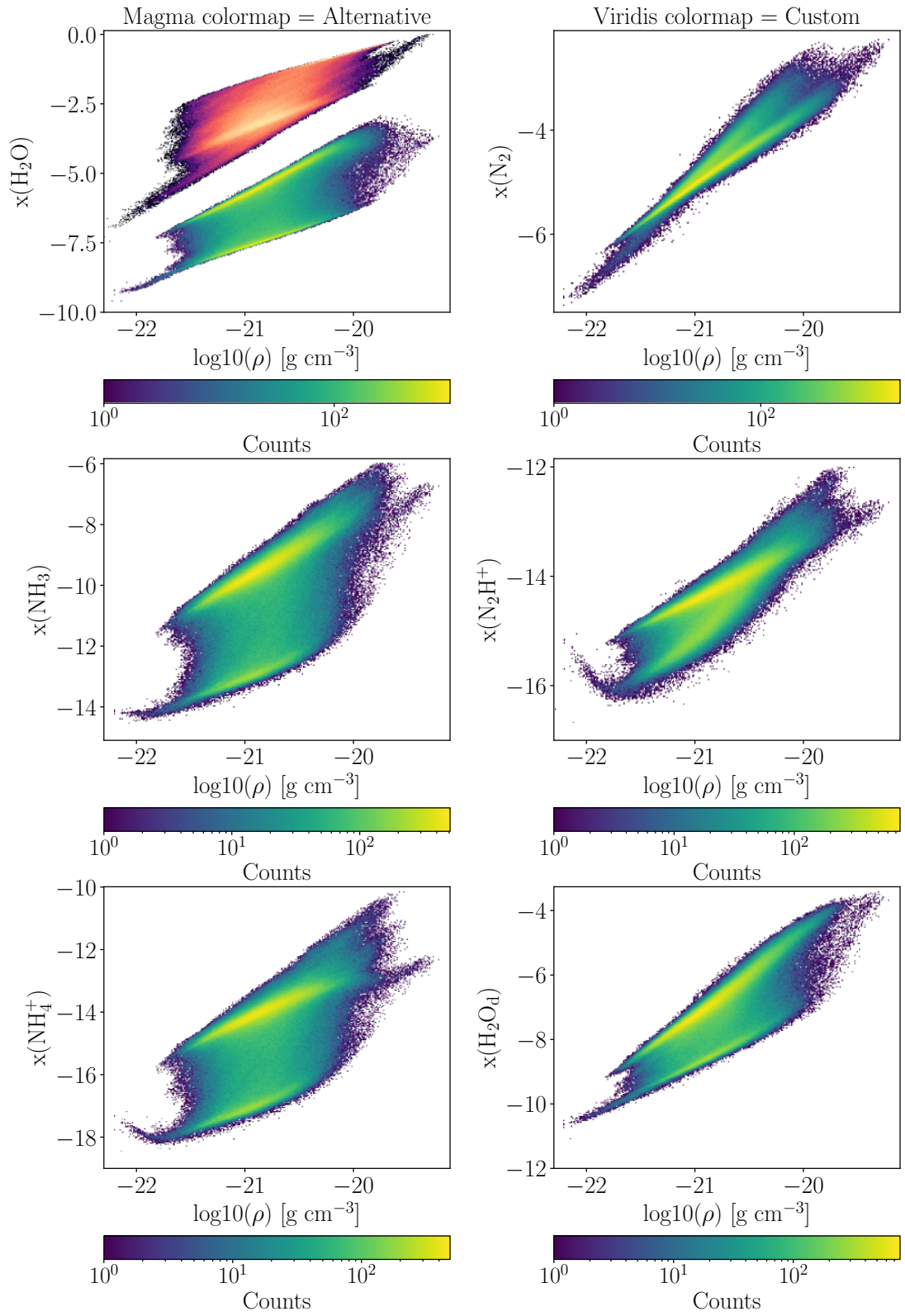

Figure 4.0.20: Analogously to Fig. (4.0.19), but without the distribution from the alternative network. The species shown are HCO^+, N_2, NH_3, N_2H^+, NH_4^+, H_2O_{dust}.

Chapter 5

Conclusion

In this study, a CR propagation scheme was developed, allowing for an accurate estimation of the CR ionisation rate in MHD simulations. The propagator was coupled to the MHD slow-collapsing prestellar core simulations Bovino et al. (2019) performed with GIZMO by implementing an interpolation scheme of gas properties consistent with the smoothing kernel procedure originally used in the simulation. The propagator traces and maps CRs as a flux of TPs, tracking the effective column density traversed by following the MF lines, and computed using the fourth-order Runge-Kutta integrator. The CR ionisation rate is then estimated at the location of each TP according to the $\mathscr{H}$ and $\mathscr{L}$ models from Padovani et al. (2018), and subsequently deposited onto the gas tracers of the original simulation in a self-consistent way. The output of the propagator was used to assess its impact on the chemistry by examining the evolution of several ions sensitive to the variable CR ionisation rate.

The scheme was tested to determine the optimal number of TPs that balance accuracy and performance. The appropriate number, 10.240 TPs, probed to be adequate enough to generate a reliable characterisation of the CR ionisation rate of the object, as demonstrated by the comparison with the most expensive run (32 times more TPs), which showed only minimal differences mostly confined to the background region.

Once the optimal number of TPs was found, the time evolution of the chemistry in the aforementioned simulation was analysed by employing the KROME library in post-processing, following the method described by Ferrada-Chamorro et al.

(2021), and coupled with the CR ionisation rate obtained from the propagator scheme. Two variable CR ionisation rate models ($\mathscr{H}$ and $\mathscr{L}$ from Padovani et al. (2018)), along with a reference constant case with $\zeta_2 = 2.5 \times 10^{-17}$ s^{-1}, were employed to assess the CR propagation impact on the chemistry.

When a proper CR propagation scheme is considered for chemical evolution, it can lead to significant, non-linear differences for key chemical tracers, particularly for deuterated species such as DCO^+ and N_2D^+. Furthermore, the correlations between the electron abundance $X(e^-)$ and ζ_2, as well as the column density of the most relevant positive ions, were examined, given the expected link between the ionisation fraction, the ionisation rate, and the abundance of positive ions. In both cases, clear correlations exist, with the two variable CR ionisation rate models exhibiting only a different normalisation. Both correlations were then fitted, providing an analytical expression for estimating the electron abundance in star-forming regions, with a standard deviation of 0.6. Additionally, the search for correlations between the local gas number density ($n(H_2)$) inherent to the simulation and the CR ionisation rate from the propagator scheme was also examined. Both distributions exhibit clear linear correlations, which were best-fitted, yielding different expressions with an uncertainty of $\sim 25\%$, intended for use in numerical simulations lacking a CR propagator scheme to estimate ζ_2 from local properties.

The analytical expression for the electron abundance was applied to a sample of 20 prestellar low-mass cores observed with APEX, making use of previous total column density maps from Herschel. We found that the ionisation fraction of most of the cores is consistent with results from the literature. Moreover, these values were used to calculate lower limits on their dynamical stability by computing the ambipolar diffusion and free-fall timescales, with the former being consistent with or greater than the latter.

A new chemical network accounting for gas-phase, solid-phase, and uni-reactions was built, with accurate rate coefficients, replacing extinction-based ones for photoreactions. It was subjected to a pair of tests under MC conditions and constant temperatures of 10 and 100 K to evaluate the time evolution of species in cool and warm gas, respectively, and to compare against the literature. Overall, the results in the two tests are positive, with some species exhibiting remarkable

agreement and only three species (H_2O, HCO^+, NH_3) differing considerable.

The thermal evolution produced by the new chemical network accounting for various cooling and heating mechanisms, was tested. The resultant temperature profile is very similar to that of Omukai et al. (2005), while also accurately including photoreactions and several other cooling and heating mechanisms not included in the original study. Therefore, this chemical network is suitable for use in further simulations of giant molecular clouds.

The custom network was employed in a numerical radiative magnetohydrodynamic simulation of a giant molecular cloud performed with STARFORGE-KROME, along with the implementation of detailed microphysics in the simulation provided by heating and cooling mechanisms built into the chemical network. Due to this, the complete chemical state of the gas cloud is revealed through non-ideal calculations, which are sufficient to account for the reactions found in the ISM and the accurate thermal evolution of the gas throughout the simulation.

Several column density maps of key species were presented, unveiling and unravelling the chemical distribution underlying the total column density, where likely next sites for star formation were identified. Finally, the abundance profile of several key species were compared with those obtained using an alternative network under equivalent conditions. The resulting 2D distributions show overall reasonable agreement, with the only exception being methane, whose low abundance makes it negligible at this stage.

Bibliography

Bakes, E. L. O. and Tielens, A. G. G. M. (1994). The Photoelectric Heating Mechanism for Very Small Graphitic Grains and Polycyclic Aromatic Hydrocarbons. , 427:822.

Ballesteros-Paredes, J., Klessen, R. S., Mac Low, M. M., and Vazquez-Semadeni, E. (2007). Molecular Cloud Turbulence and Star Formation. In Reipurth, B., Jewitt, D., and Keil, K., editors, *Protostars and Planets V*, page 63.

Barger, C. J. and Garrod, R. T. (2020). Constraining Cosmic-Ray Ionization Rates and Chemical Timescales in Massive Hot Cores. , 888(1):38.

Bate, M. R., Bonnell, I. A., and Bromm, V. (2003). The formation of a star cluster: predicting the properties of stars and brown dwarfs. , 339(3):577–599.

Bate, M. R., Bonnell, I. A., and Price, N. M. (1995). Modelling accretion in protobinary systems. , 277(2):362–376.

Bergin, E. A. and Tafalla, M. (2007). Cold Dark Clouds: The Initial Conditions for Star Formation. , 45(1):339–396.

Bialy, Shmuel, Belli, Sirio, and Padovani, Marco (2022). Constraining the cosmic-ray ionization rate and spectrum with nir spectroscopy of dense clouds - a testbed for jwst. *AA*, 658:L13.

Bovino, S., Ferrada-Chamorro, S., Lupi, A., Sabatini, G., Giannetti, A., and Schleicher, D. R. G. (2019). The 3D Structure of CO Depletion in High-mass Prestellar Regions. , 887(2):224.

Bovino, S., Ferrada-Chamorro, S., Lupi, A., Schleicher, D. R. G., and Caselli, P. (2020). A new proxy to estimate the cosmic ray ionization rate in dense cores. , 495(1):L7–L11.

Bovino, S., Lupi, A., Giannetti, A., Sabatini, G., Schleicher, D. R. G., Wyrowski, F., and Menten, K. M. (2021). Chemical analysis of prestellar cores in Ophiuchus yields short timescales and rapid collapse. , 654:A34.

Bustard, C. and Zweibel, E. G. (2021). Cosmic-Ray Transport, Energy Loss, and Influence in the Multiphase Interstellar Medium. , 913(2):106.

Calzetti, D., Armus, L., Bohlin, R. C., Kinney, A. L., Koornneef, J., and Storchi-Bergmann, T. (2000). The Dust Content and Opacity of Actively Star-forming Galaxies. , 533(2):682–695.

Caselli, P., Walmsley, C. M., Terzieva, R., and Herbst, E. (1998). The Ionization Fraction in Dense Cloud Cores. , 499(1):234–249.

Caselli, P., Walmsley, C. M., Zucconi, A., Tafalla, M., Dore, L., and Myers, P. C. (2002). Molecular Ions in L1544. II. The Ionization Degree. , 565(1):344–358.

Ceccarelli, C., Dominik, C., Lefloch, B., Caselli, P., and Caux, E. (2004). Detection of H_2D^+: Measuring the Midplane Degree of Ionization in the Disks of DM Tauri and TW Hydrae. , 607(1):L51–L54.

Ceccarelli, C., Dominik, C., López-Sepulcre, A., Kama, M., Padovani, M., Caux, E., and Caselli, P. (2014). Herschel Finds Evidence for Stellar Wind Particles in a Protostellar Envelope: Is This What Happened to the Young Sun? , 790(1):L1.

Cen, R. (1992). A Hydrodynamic Approach to Cosmology: Methodology. , 78:341.

Chan, T. K., Kereš, D., Hopkins, P. F., Quataert, E., Su, K. Y., Hayward, C. C., and Faucher-Giguère, C. A. (2019). Cosmic ray feedback in the FIRE simulations: constraining cosmic ray propagation with GeV γ-ray emission. , 488(3):3716–3744.

Crutcher, R. M. (2012). Magnetic Fields in Molecular Clouds. , 50:29–63.

Cunningham, A. J., Klein, R. I., Krumholz, M. R., and McKee, C. F. (2011). Radiation-hydrodynamic Simulations of Massive Star Formation with Protostellar Outflows. , 740(2):107.

de Boisanger, C., Helmich, F. P., and van Dishoeck, E. F. (1996). The ionization fraction in dense clouds. , 310:315–327.

Federrath, C., Banerjee, R., Clark, P. C., and Klessen, R. S. (2010). Modeling Collapse and Accretion in Turbulent Gas Clouds: Implementation and Comparison of Sink Particles in AMR and SPH. , 713(1):269–290.

Ferrada-Chamorro, S., Lupi, A., and Bovino, S. (2021). Chemical post-processing of magneto-hydrodynamical simulations of star-forming regions: robustness and pitfalls. , 505(3):3442–3451.

Flower, D. R., Pineau des Forêts, G., and Walmsley, C. M. (2004). Multiply-deuterated species in prestellar cores. , 427:887–893.

Flower, D. R., Pineau Des Forêts, G., and Walmsley, C. M. (2006). The importance of the ortho:para H_2 ratio for the deuteration of molecules during pre-protostellar collapse. , 449(2):621–629.

Fuente, A., Cernicharo, J., Roueff, E., Gerin, M., Pety, J., Marcelino, N., Bachiller, R., Lefloch, B., Roncero, O., and Aguado, A. (2016). Ionization fraction and the enhanced sulfur chemistry in Barnard 1. , 593:A94.

Gaches, B. A. L., Bisbas, T. G., and Bialy, S. (2022). The impact of cosmic-ray attenuation on the carbon cycle emission in molecular clouds. , 658:A151.

Galli, D. and Padovani, M. (2015). Cosmic-ray heating of molecular cloud cores. *arXiv e-prints*, page arXiv:1502.03380.

Galli, D. and Palla, F. (1998). The chemistry of the early Universe. , 335:403–420.

Garrod, R. T. and Herbst, E. (2006). Formation of methyl formate and other organic species in the warm-up phase of hot molecular cores. , 457(3):927–936.

Gavilan, L., Vidali, G., Lemaire, J. L., Chehrouri, M., Dulieu, F., Fillion, J. H., Congiu, E., and Chaabouni, H. (2012). Experimental Investigation of the Ortho/Para Ratio of Newly Formed Molecular Hydrogen on Amorphous Solid Water. , 760(1):35.

Glassgold, A. E., Galli, D., and Padovani, M. (2012). Cosmic-Ray and X-Ray Heating of Interstellar Clouds and Protoplanetary Disks. , 756(2):157.

Glover, S. C. O. and Abel, T. (2008). Uncertainties in H_2 and HD chemistry and cooling and their role in early structure formation. , 388(4):1627–1651.

Glover, S. C. O., Federrath, C., Mac Low, M. M., and Klessen, R. S. (2010). Modelling CO formation in the turbulent interstellar medium. , 404(1):2–29.

Grassi, T., Bovino, S., Gianturco, F. A., Baiocchi, P., and Merlin, E. (2012). Complexity reduction of astrochemical networks. , 425(2):1332–1340.

Grassi, T., Bovino, S., Haugbølle, T., and Schleicher, D. R. G. (2017). A detailed framework to incorporate dust in hydrodynamical simulations. , 466(2):1259–1274.

Grassi, T., Bovino, S., Schleicher, D. R. G., Prieto, J., Seifried, D., Simoncini, E., and Gianturco, F. A. (2014). KROME - a package to embed chemistry in astrophysical simulations. , 439(3):2386–2419.

Grassi, T., Merlin, E., Piovan, L., Buonomo, U., and Chiosi, C. (2011). MaNN: Multiple Artificial Neural Networks for modelling the Interstellar Medium. *arXiv e-prints*, page arXiv:1103.0509.

Grudić, M. Y., Guszejnov, D., Hopkins, P. F., Offner, S. S. R., and Faucher-Giguère, C.-A. (2021). STARFORGE: Towards a comprehensive numerical model of star cluster formation and feedback. , 506(2):2199–2231.

Hasegawa, T. and Umemura, M. (1993). Luminosity dependence of galaxy clustering in extinction-corrected CfA data. , 263(1):191–210.

Hasegawa, T. I., Herbst, E., and Leung, C. M. (1992). Models of Gas-Grain Chemistry in Dense Interstellar Clouds with Complex Organic Molecules. , 82:167.

Heays, A. N., Bosman, A. D., and van Dishoeck, E. F. (2017). Photodissociation and photoionisation of atoms and molecules of astrophysical interest. , 602:A105.

Hennebelle, P. and Inutsuka, S.-i. (2019). The role of magnetic field in molecular cloud formation and evolution. *Frontiers in Astronomy and Space Sciences*, 6:5.

Hezareh, T., Houde, M., McCoey, C., Vastel, C., and Peng, R. (2008). Simultaneous Determination of the Cosmic Ray Ionization Rate and Fractional Ionization in DR 21(OH). , 684(2):1221–1227.

Hollenbach, D. and McKee, C. F. (1979). Molecule formation and infrared emission in fast interstellar shocks. I. Physical processes. , 41:555–592.

Hopkins, P. F. (2015). A new class of accurate, mesh-free hydrodynamic simulation methods. , 450(1):53–110.

Hopkins, P. F., Grudić, M. Y., Wetzel, A., Kereš, D., Faucher-Giguère, C.-A., Ma, X., Murray, N., and Butcher, N. (2020). Radiative stellar feedback in galaxy formation: Methods and physics. , 491(3):3702–3729.

Hopkins, P. F., Narayanan, D., and Murray, N. (2013). The meaning and consequences of star formation criteria in galaxy models with resolved stellar feedback. , 432(4):2647–2653.

Hopkins, P. F. and Raives, M. J. (2016). Accurate, meshless methods for magnetohydrodynamics. , 455(1):51–88.

Hopkins, P. F., Wetzel, A., Kereš, D., Faucher-Giguère, C.-A., Quataert, E., Boylan-Kolchin, M., Murray, N., Hayward, C. C., and El-Badry, K. (2018). How to model supernovae in simulations of star and galaxy formation. , 477(2):1578–1603.

Indriolo, N. and McCall, B. J. (2012). Investigating the Cosmic-Ray Ionization Rate in the Galactic Diffuse Interstellar Medium through Observations of H^+_3. , 745(1):91.

Klessen, R. S. and Burkert, A. (2000). The Formation of Stellar Clusters: Gaussian Cloud Conditions. I. , 128(1):287–319.

Krumholz, M. R. (2015). Notes on Star Formation. *arXiv e-prints*, page arXiv:1511.03457.

Lamers, H. J. G. L. M., Snow, T. P., and Lindholm, D. M. (1995). Terminal Velocities and the Bistability of Stellar Winds. , 455:269.

Larson, R. B. (1981). Turbulence and star formation in molecular clouds. , 194:809–826.

Leger, A., Jura, M., and Omont, A. (1985). Desorption from interstellar grains. , 144(1):147–160.

Lupi, A., Bovino, S., and Grassi, T. (2021). On the low ortho-to-para H_2 ratio in star-forming filaments. , 654:L6.

Maret, S. and Bergin, E. A. (2007). The Ionization Fraction of Barnard 68: Implications for Star and Planet Formation. , 664(2):956–963.

Morales Ortiz, J. L., Ceccarelli, C., Lis, D. C., Olmi, L., Plume, R., and Schilke, P. (2014). Ionization toward the high-mass star-forming region NGC 6334 I. , 563:A127.

Neufeld, D. A. and Wolfire, M. G. (2017). The Cosmic-Ray Ionization Rate in the Galactic Disk, as Determined from Observations of Molecular Ions. , 845(2):163.

Ogrodnik, M. A., Hanasz, M., and Wóltański, D. (2021). Implementation of Cosmic Ray Energy Spectrum (CRESP) Algorithm in PIERNIK MHD Code. I. Spectrally Resolved Propagation of Cosmic Ray Electrons on Eulerian Grids. , 253(1):18.

Oka, T. (2004). Nuclear spin selection rules in chemical reactions by angular momentum algebra. *Journal of Molecular Spectroscopy*, 228(2):635–639.

Omukai, K. (2000). Protostellar Collapse with Various Metallicities. , 534(2):809–824.

Omukai, K., Tsuribe, T., Schneider, R., and Ferrara, A. (2005). Thermal and Fragmentation Properties of Star-forming Clouds in Low-Metallicity Environments. , 626(2):627–643.

Padovani, M., Bialy, S., Galli, D., Ivlev, A. V., Grassi, T., Scarlett, L. H., Rehill, U. S., Zammit, M. C., Fursa, D. V., and Bray, I. (2022). Cosmic rays in molecular clouds probed by H_2 rovibrational lines. Perspectives for the James Webb Space Telescope. , 658:A189.

Padovani, M., Galli, D., and Glassgold, A. E. (2009). Cosmic-ray ionization of molecular clouds. , 501(2):619–631.

Padovani, M., Hennebelle, P., and Galli, D. (2013). Cosmic-ray ionisation in collapsing clouds. , 560:A114.

Padovani, M., Ivlev, A. V., Galli, D., and Caselli, P. (2018). Cosmic-ray ionisation in circumstellar discs. , 614:A111.

Pagani, L., Vastel, C., Hugo, E., Kokoouline, V., Greene, C. H., Bacmann, A., Bayet, E., Ceccarelli, C., Peng, R., and Schlemmer, S. (2009). Chemical modeling of <ASTROBJ>L183</ASTROBJ> (<ASTROBJ>L134N</ASTROBJ>): an estimate of the ortho/para H{_2} ratio. , 494(2):623–636.

Redaelli, E., Bizzocchi, L., Caselli, P., Harju, J., Chacón-Tanarro, A., Leonardo, E., and Dore, L. (2018). $^{14}N/^{15}N$ ratio measurements in prestellar cores with N_2H^+: new evidence of ^{15}N-antifractionation. , 617:A7.

Redaelli, E., Bovino, S., Sabatini, G., Arzoumanian, D., Padovani, M., Caselli, P., Wyrowski, F., Pineda, J. E., and Latrille, G. (2025). Cosmic-ray ionisation rate in low-mass cores: The role of the environment. , 702:A210.

Redaelli, E., Sipilä, O., Padovani, M., Caselli, P., Galli, D., and Ivlev, A. V. (2021). The cosmic-ray ionisation rate in the pre-stellar core L1544. , 656:A109.

Ripamonti, E. and Abel, T. (2004). Fragmentation and the formation of primordial protostars: the possible role of collision-induced emission. , 348(3):1019–1034.

Sabatini, G., Bovino, S., Giannetti, A., Wyrowski, F., Órdenes, M. A., Pascale, R., Pillai, T., Wienen, M., Csengeri, T., and Menten, K. M. (2020). Survey of ortho-H_2D^+ in high-mass star-forming regions. , 644:A34.

Sabatini, G., Bovino, S., and Redaelli, E. (2023). First ALMA Maps of Cosmic-Ray Ionization Rate in High-mass Star-forming Regions. , 947(1):L18.

Schinnerer, E. and Leroy, A. K. (2024). Molecular Gas and the Star-Formation Process on Cloud Scales in Nearby Galaxies. , 62(1):369–436.

Semenov, D., Hersant, F., Wakelam, V., Dutrey, A., Chapillon, E., Guilloteau, S., Henning, T., Launhardt, R., Piétu, V., and Schreyer, K. (2010). Chemistry in disks. IV. Benchmarking gas-grain chemical models with surface reactions. , 522:A42.

Shaw, G., Ferland, G. J., Srianand, R., Abel, N. P., van Hoof, P. A. M., and Stancil, P. C. (2008). On the Enhanced Cosmic-Ray Ionization Rate in the Diffuse Cloud toward ζ Persei. , 675(1):405–412.

Shu, F. H., Adams, F. C., and Lizano, S. (1987). Star formation in molecular clouds: observation and theory. , 25:23–81.

Silsbee, K., Ivlev, A. V., Padovani, M., and Caselli, P. (2018). Magnetic Mirroring and Focusing of Cosmic Rays. , 863(2):188.

Sipilä, O., Caselli, P., and Harju, J. (2015). Benchmarking spin-state chemistry in starless core models. , 578:A55.

Snow, T. P. and McCall, B. J. (2006). Diffuse Atomic and Molecular Clouds. , 44(1):367–414.

Spezzano, S., Caselli, P., Bizzocchi, L., Giuliano, B. M., and Lattanzi, V. (2017). The observed chemical structure of L1544. , 606:A82.

Spitzer, L. (1978). *Physical processes in the interstellar medium.*

Su, T. and Chesnavich, W. J. (1982). Parametrization of the ion-polar molecule collision rate constant by trajectory calculations. , 76(10):5183–5185.

Thomas, T., Pfrommer, C., and Pakmor, R. (2021). A finite volume method for two-moment cosmic ray hydrodynamics on a moving mesh. , 503(2):2242–2264.

Tielens, A. (2005). *The Physics and Chemistry of the Interstellar Medium*. Cambridge University Press.

Torrey, P., Hopkins, P. F., Faucher-Giguère, C.-A., Anglés-Alcázar, D., Quataert, E., Ma, X., Feldmann, R., Keres, D., and Murray, N. (2020). The impact of AGN wind feedback in simulations of isolated galaxies with a multiphase ISM. , 497(4):5292–5308.

van der Tak, F. F. S., van Dishoeck, E. F., Evans, II, N. J., and Blake, G. A. (2000). Structure and Evolution of the Envelopes of Deeply Embedded Massive Young Stars. , 537(1):283–303.

Wakelam, V., Herbst, E., Loison, J. C., Smith, I. W. M., Chandrasekaran, V., Pavone, B., Adams, N. G., Bacchus-Montabonel, M. C., Bergeat, A., Béroff, K., Bierbaum, V. M., Chabot, M., Dalgarno, A., van Dishoeck, E. F., Faure, A., Geppert, W. D., Gerlich, D., Galli, D., Hébrard, E., Hersant, F., Hickson, K. M., Honvault, P., Klippenstein, S. J., Le Picard, S., Nyman, G., Pernot, P., Schlemmer, S., Selsis, F., Sims, I. R., Talbi, D., Tennyson, J., Troe, J., Wester, R., and Wiesenfeld, L. (2012). A KInetic Database for Astrochemistry (KIDA). , 199(1):21.

Winner, G., Pfrommer, C., Girichidis, P., and Pakmor, R. (2019). Evolution of cosmic ray electron spectra in magnetohydrodynamical simulations. , 488(2):2235–2252.

Wolfire, M. G., Hollenbach, D., McKee, C. F., Tielens, A. G. G. M., and Bakes, E. L. O. (1995). The Neutral Atomic Phases of the Interstellar Medium. , 443:152.